The Astrophysical Journal, 656:1223–1240, 2007 February 20


# CHARACTERIZATION OF PRESOLAR SILICATE AND OXIDE GRAINS IN PRIMITIVE CARBONACEOUS CHONDRITES

Ann N. Nguyen,[1,2] Frank J. Stadermann,[1] Ernst Zinner,[1] Rhonda M. Stroud,[3]
Conel M. O'D. Alexander,[4] and Larry R. Nittler[4]
*Received 2006 July 14; accepted 2006 November 2*

## ABSTRACT

Raster ion imaging of the oxygen isotopes with the NanoSIMS ion microprobe has been used to identify presolar grains in two primitive meteorites. Eleven presolar silicates and eight presolar oxides were identified in the primitive carbonaceous chondrite Acfer 094 for abundances of 325 and 360 parts per million (ppm), respectively. In addition, nine presolar silicates and five presolar oxide grains were identified in the CO3 chondrite ALHA 77307, for abundances of 320 and 200 ppm, respectively. These abundances, which are matrix-normalized and corrected for instrumental detection efficiencies, are much higher than those of other presolar phases, with the exception of nanodiamonds, although the latter may not all be presolar. The chemical compositions of six presolar silicate grains from ALHA 77307 were elucidated by Auger spectroscopy. Transmission electron microscopy (TEM) analysis of one presolar silicate grain revealed a nonstoichiometric composition and an amorphous structure as indicated by the diffuse electron diffraction pattern. The oxygen isotopic compositions of the presolar silicates indicate origins in red giant and asymptotic giant branch stars. Analysis of the Si isotopic compositions of 10 presolar silicates provides further constraints on the effects of Galactic chemical evolution.

*Subject headings:* circumstellar matter — dust, extinction — Galaxy: evolution — nuclear reactions, nucleosynthesis, abundances — stars: evolution

## 1. INTRODUCTION

Dust grains that condensed in the atmospheres of evolved stars and in nova and supernova ejecta are preserved in primitive meteorites, interplanetary dust particles (IDPs), and Antarctic micrometeorites (AMMs; Nittler 2003; Zinner 2004; Yada et al. 2005, 2006). These grains have been minimally altered since their formation and conserve the exotic isotopic signatures of their parent stars, which differ dramatically from the isotopic compositions of any solar system materials. In studying stardust, we can elucidate the intricacies of stellar evolution and nucleosynthesis and Galactic chemical evolution (GCE) to a degree that cannot be achieved by astronomical observations alone.

The first presolar grains discovered were carbonaceous phases: presolar diamond (Lewis et al. 1987), SiC (Bernatowicz et al. 1987), and graphite (Amari et al. 1990). Presolar oxide grains are more difficult to identify, because meteoritic material is dominated by O-rich phases that originated in the solar system. Despite this background of oxide grains having "normal" isotopic composition, anomalous oxide grains, including presolar corundum ($Al_2O_3$; Huss et al. 1994; Hutcheon et al. 1994; Nittler et al. 1994, 1997, 1998; Strebel et al. 1996; Choi et al. 1998, 1999; Nittler & Alexander 1999; Krestina et al. 2002), spinel ($MgAl_2O_4$; Nittler et al. 1994, 1997; Choi et al. 1998; Nittler & Alexander 1999; Nguyen et al. 2003; Zinner et al. 2003, 2005), hibonite ($CaAl_{12}O_{19}$; Choi et al. 1999; Krestina et al. 2002; Nittler et al. 2005a), and $TiO_2$ (Nittler & Alexander 1999; Nittler et al. 2005a), have been identified. Most of these presolar oxides condensed around O-rich evolved stars. Although astronomical observations indicate that submicrometer-sized amorphous and crystalline silicate grains, rather than oxide grains, are the most abundant grain species in the environments of young main-sequence stars (Waelkens et al. 1996; Malfait et al. 1998) and O-rich evolved stars (Waters et al. 1996; Demyk et al. 2000), presolar silicates were only recently discovered in IDPs (Messenger et al. 2003) and primitive meteorites (Nagashima et al. 2004; Nguyen & Zinner 2004).

There are several experimental challenges involved in finding isotopically anomalous silicate grains in meteorites. Silicate grains are more susceptible to destruction by processing in the solar nebula or parent body than other refractory presolar phases. As such, the very primitive meteorites (i.e., those that have largely escaped aqueous alteration and thermal metamorphism) are most likely to harbor these fragile grains. In addition, presolar silicates are prone to being obscured by the plethora of silicate grains that have compositions indistinguishable from the average compositions of solar system materials. In other words, a large number of grains must be analyzed in order to find the few isotopically anomalous ones. These difficulties are exacerbated by the submicron sizes of most presolar silicate grains and the limiting spatial resolution (>1 $\mu$m) of traditional ion microprobes, the instrument of choice for locating presolar grains.

These complications can be addressed by taking advantage of the novel capabilities of the NanoSIMS 50 ion probe (Cameca Instruments). The high spatial resolution and sensitivity of this instrument allow for the isotopic measurement of single grains down to 0.1 $\mu$m diameter (Zinner et al. 2003). Furthermore, individual anomalous submicron grains can be identified while packed in among grains of solar system origin by way of multidetection raster ion imaging (Nguyen et al. 2003). The discovery of presolar silicates in meteorites was achieved by raster ion imaging of tightly packed size-separated grains from the primitive meteorite Acfer 094 in the NanoSIMS (Nguyen & Zinner 2004). Since then, presolar silicates have been identified in other meteorites as well (Mostefaoui et al. 2003, 2004; Mostefaoui & Hoppe 2004; Nagashima et al. 2004, 2005; Kobayashi et al. 2005; Stadermann

[1] Laboratory for Space Sciences and Physics Department, Washington University, St. Louis, MO.
[2] Current address: Department of Terrestrial Magnetism, Carnegie Institution of Washington, Washington, DC; nguyen@dtm.ciw.edu.
[3] Materials and Sensors Branch, Naval Research Laboratory, Washington, DC.
[4] Department of Terrestrial Magnetism, Carnegie Institution of Washington, Washington, DC.

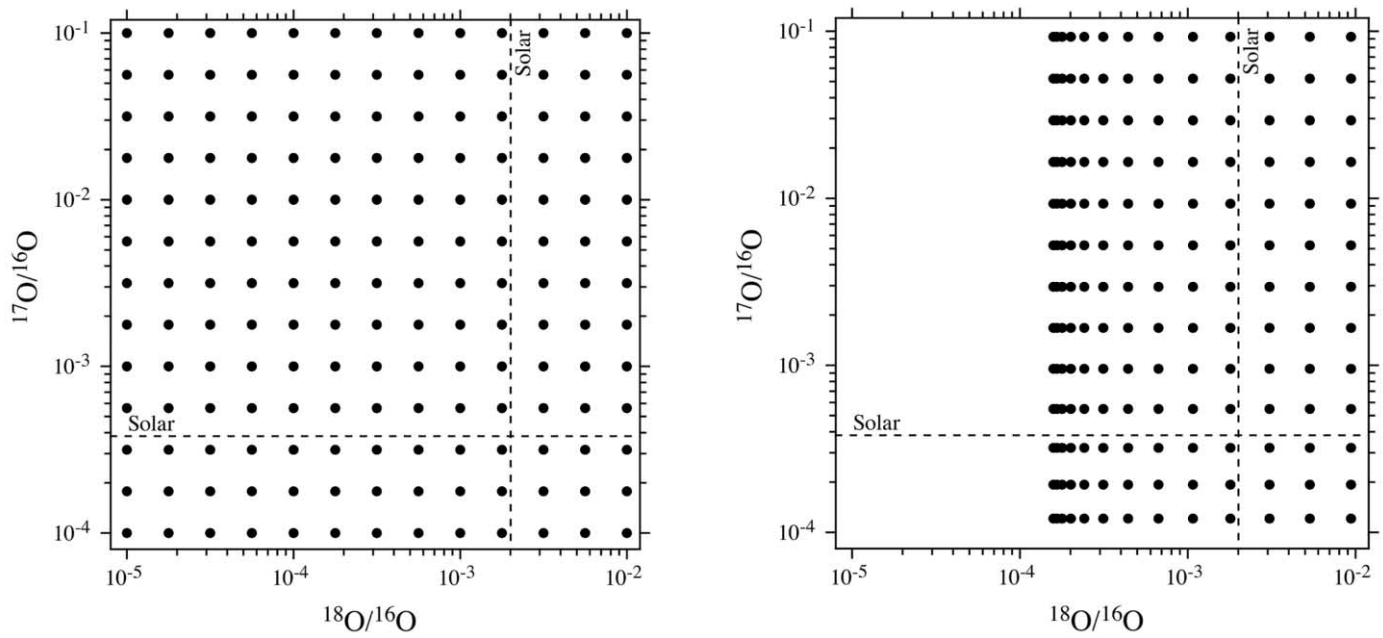


FIG. 1.—Assumed oxygen isotopic ratios (*left*) and ratios obtained by computer-simulated raster imaging analysis (*right*) of tightly packed grains, where individual anomalous grains are surrounded by isotopically normal grains. The dashed lines indicate the solar ratios for $^{17}O/^{16}O$ and $^{18}O/^{16}O$. Simulation parameters: grain size 150 nm, primary beam size 100 nm, and raster step size 40 nm.

et al. 2005a; Ebata et al. 2006; Marhas et al. 2006; Tonotani et al. 2006; Vollmer et al. 2006). Here, we report on further searches of presolar silicate grains and presolar oxide grains, as well as additional isotopic and chemical analyses of them.

## 2. EXPERIMENTAL

Nguyen & Zinner (2004) identified presolar silicate grains in a size-separated sample containing matrix grains 100–500 nm in diameter from the primitive carbonaceous chondrite Acfer 094. In the present study the search for presolar silicate grains in meteorites was extended to another grain size separate of Acfer 094 containing grains 0.5–1 $\mu$m in diameter, as well as to polished meteorite thin sections of Acfer 094 and the CO3 chondrite ALHA 77307. Densely packed areas on the grain dispersion mounts and matrix areas on the thin sections were chosen for analysis by multidetection raster ion imaging with the Cameca NanoSIMS 50 at Washington University. A typical measurement involved rastering a focused ($\sim$100–200 nm) primary $Cs^+$ beam of a few pA over $20 \times 20$ $\mu m^2$ areas ($256 \times 256$ pixels) for 20–40 scans. The three oxygen isotopes, $^{24}Mg^{16}O$, and $^{28}Si$ were measured as negative secondary ions simultaneously in five electron multipliers. Secondary electrons were detected along with the secondary ions. The ion images allow for the identification of grains having anomalous O isotopic ratios, and in most cases they also enable the differentiation of silicates from oxides on the basis of the correlated $^{24}Mg^{16}O^-$ and $^{28}Si^-$ signals. Limited identification of the mineralogy of the oxide grains can be obtained from their $^{24}Mg^{16}O^-/^{16}O^-$ ratios. For example, the presence of Mg indicates spinel, but its absence could indicate another oxide phase, most likely either corundum or hibonite.

In a separate measurement sequence, the three Si isotopes, along with $^{16}O$ and $^{18}O$, were subsequently measured simultaneously as negative secondary ions for 10 anomalous silicate grains from a size separate and a thin section of Acfer 094. For these measurements, a $Cs^+$ primary beam was rastered over $10 \times 10$ $\mu m^2$ areas around the anomalous grains and $128 \times 128$ pixel images were acquired. By far, most analyzed grains have "normal" isotopic compositions, which are indistinguishable from the compositions of materials of solar system origin. The $^{17}O/^{16}O$ and $^{18}O/^{16}O$, and $^{29}Si/^{28}Si$ and $^{30}Si/^{28}Si$ ratios of anomalous grains are therefore normalized to the average ratios of the isotopically normal grains in the analyzed areas.

Comparison of O isotopic measurements of small spatially separated grains (Zinner et al. 2003, 2005) with isotopic imaging measurements of tightly packed grains (Nguyen et al. 2003) showed two distinct effects. First, the detection efficiency of isotopically anomalous grains is lower during imaging analysis than during isolated-grain analysis and depends on grain size. Whereas the abundances of presolar spinel grains in the Murray separates CF (average grain size 0.15 $\mu$m) and CG (average grain size 0.45 $\mu$m; Tang & Anders 1988) are 2.4% (15/628) and 1.7% (21/1253), respectively, in isolated-grain analysis (Zinner et al. 2003, 2005), these abundances are 0.16% and 0.9%, respectively, in isotopic imaging analysis of tightly packed grains (Nguyen et al. 2003). Second, O isotopic ratios measured by isotopic imaging are shifted toward normal ratios when compared with those measured in isolated grains (Nguyen et al. 2003). Both effects are undoubtedly due to overlap of the primary beam onto adjacent, isotopically normal grains, which dilutes the measured isotopic compositions of the anomalous grains.

In order to investigate this dilution effect more systematically, we performed computer simulations of raster imaging measurements on tightly packed grains. The grains were represented as circles of identical size, and the primary beam was assumed to be a circle with uniform current density. Anomalous grains were assumed to be packed in with isotopically normal grains. In addition to grain and beam diameter, other parameters that could be varied were the raster step size, the offset of the raster grid relative to the grain position grid, and the number of measurement pixels that were binned to obtain a measurement point. Results of simulations are shown in Figures 1 and 2. Figure 1 shows the measured O isotopic ratios (*right*) compared to the original ratios (*left*), which were assumed to cover the log-log O three-isotope plot in a uniform grid. Figure 2 shows a comparison of the original

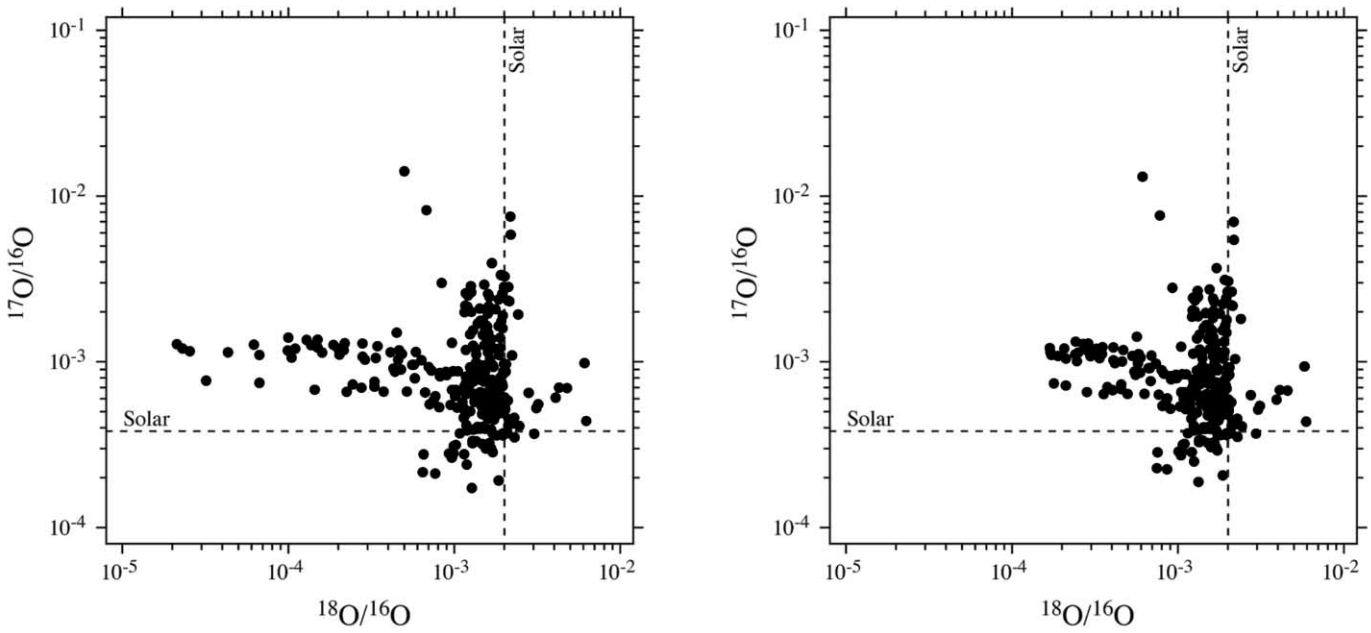


FIG. 2.—Oxygen isotopic ratios of oxide grains analyzed as single grains (*left*) and ratios obtained by computer-simulated raster imaging analysis (*right*) of the same grains assumed to be surrounded by isotopically normal grains. Simulation parameters: grain size 150 nm, primary beam size 100 nm, and raster step size 40 nm.

(*left*) and simulated (*right*) measurements of presolar oxide grains measured as isolated grains (Nittler et al. 1997, 2005a; Choi et al. 1998, 1999; Nittler & Alexander 1999; Krestina et al. 2002; Zinner et al. 2003, 2005). As can be seen, the effect of beam overlap is mostly to shift isotopic ratios with depletions in $^{17}O$ and $^{18}O$ relative to solar isotopic ratios toward the normal ratios. In contrast, the effect on ratios with excesses in $^{17}O$ and $^{18}O$ is much less pronounced. As expected, the degree to which anomalous ratios are shifted toward normal ratios increases with increasing ratio of primary beam diameter to grain diameter.

However, this simulation is only a crude first step. In reality, there are additional factors that can contribute to shifts toward normal isotopic ratios. First, the assumption of a uniform current density within a circular beam is not realistic. In fact, the primary beam of the NanoSIMS has an approximately Gaussian shape, with diameter corresponding to the full width at half-maximum (FWHM). The resulting long tails on the beam increase the dilution effects. Another factor is the low number of counts in $^{17}O$ and $^{18}O$ (especially in grains with large depletions in these isotopes), which forces us to bin several pixels in order to obtain statistically meaningful total counts. Consequently, areas at the edges of the grains having larger contributions from adjacent material are included in the data analysis. Finally, there is the possibility of shifts in the position of the rastered image from one measurement frame to the next (we analyzed 20–40 individual frames) due to drift of either the sample stage or the primary beam. Although we aligned the individual images relative to one another by autocorrelation between individual layers in order to obtain an integrated image of all frames, these positional shifts resulted in some isotopic dilutions.

To better understand the effects of the nonuniform beam shape and low counting statistics, we performed additional simulations in which synthetic NanoSIMS O isotopic images were generated assuming a Gaussian beam with FWHM = 100 nm. In each image, several presolar grains with a range of sizes and isotopic compositions were randomly placed in an otherwise homogeneous, isotopically normal medium. Individual pixel counts were randomly selected from Poisson distributions corresponding to count rates and integration times similar to those of the real measurements. The simulated images were subsequently analyzed as if they were actual NanoSIMS data (Fig. 3).

Six O isotopic compositions were assumed for simulated presolar grains (Fig. 3, *filled triangles*), representing the range of most observed presolar oxide and silicate grains. For each composition, six grain diameters ranging from 150 to 600 nm were considered

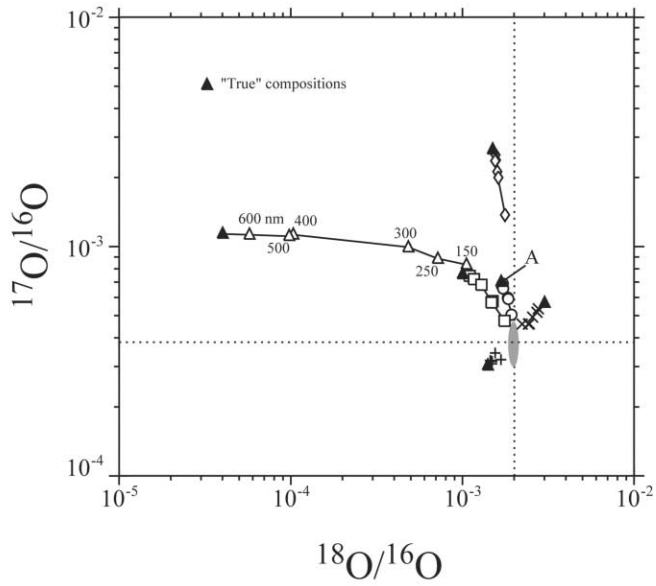


FIG. 3.—Oxygen isotopic ratios of six simulated presolar grains determined from synthetic NanoSIMS images (100 nm FWHM Gaussian primary beam). Filled triangles indicate the true compositions assumed for the presolar grains; other symbols indicate ratios determined by image processing analysis for grains of various diameters (denoted for one original isotopic composition). The composition of grain A is the approximate median composition of group 1 presolar oxide grains. Isotopic dilution from neighboring grains affects all measured compositions, but is much more severe for the smallest grains. The shaded ellipse corresponds roughly to the range of O isotopic ratios determined for isotopically normal grains in real NanoSIMS data. The dashed lines indicate the solar ratios for $^{17}O/^{16}O$ and $^{18}O/^{16}O$.

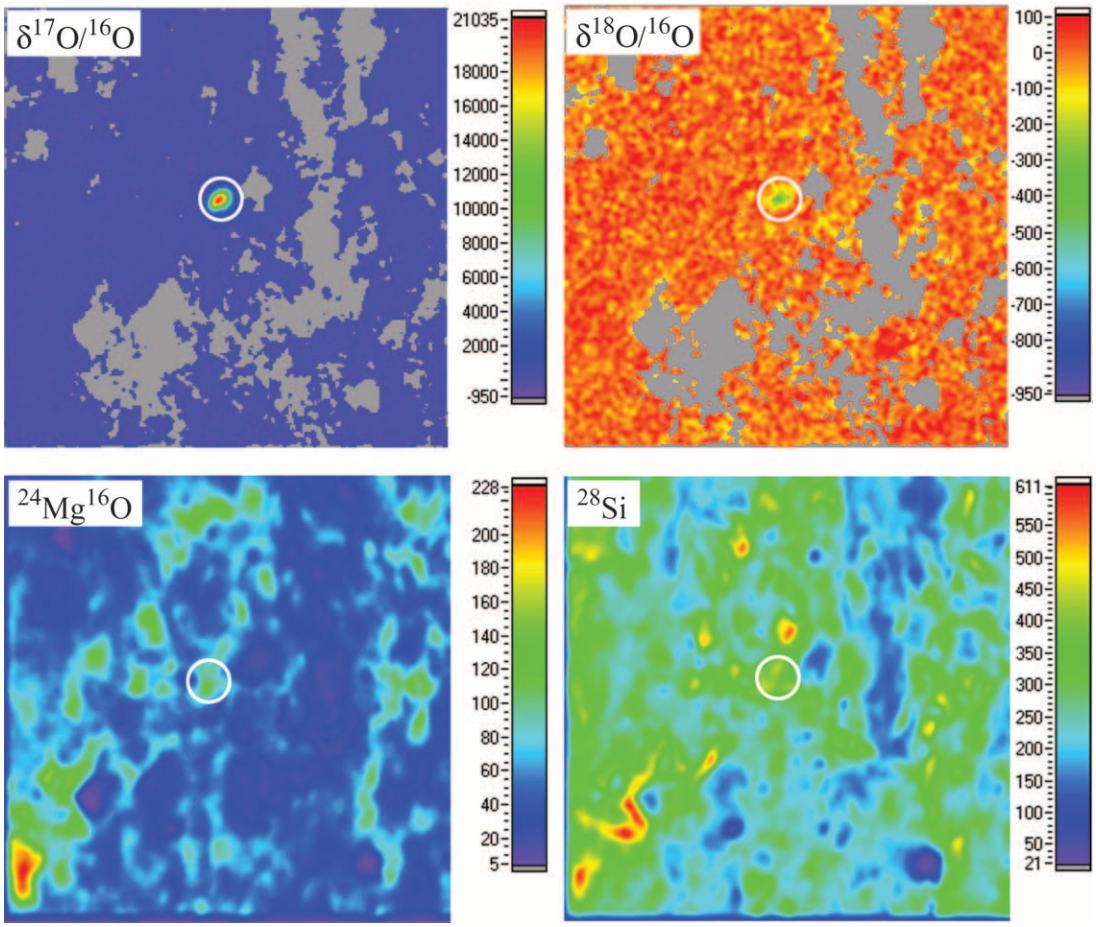


FIG. 4.—Oxygen isotopic ratio and isotopic images of a $10 \times 10$ $\mu m^2$ area containing a presolar grain (*circled*) from the Acfer 094 thin section (grain A094_TS6). The color bars for the upper two plots give the ratios as delta values ($\delta$), or deviations from solar oxygen isotopic ratios in parts per thousand (‰); those in the lower two plots give ion intensities in counts per second. Small deviations from normal isotopic composition are due to statistical fluctuations. However, the presolar grain has a much larger anomaly. Ion images of $^{24}Mg^{16}O$ and $^{28}Si$ indicate that this is a Mg-rich silicate grain. Gray areas in the ratio images indicate regions of the sample where the counts are too low to be statistically significant; these areas were excluded from analysis.

(*other plotted symbols*). These results indicate that shifts in isotopic composition due to dilution from neighboring grains occur even in grains significantly larger than the primary beam and that for the smallest grains these shifts are much more severe than those obtained by the simpler simulations described above. It is illustrative to examine the results for grain "A" in Figure 3. The O isotopic composition of this grain is the median composition of group 1 presolar oxide grains, the largest population of presolar oxides (Nittler et al. 1997). The simulations indicate that even for 250 nm grains this composition gets shifted to a composition close to the field of isotopically normal grains (*shaded ellipse*), and a grain with this composition thus would likely not be identified as presolar in a real measurement. Since grain A has a median composition, the simulation suggests that at least 50% of typical group 1 250 nm grains are likely to be missed in raster imaging measurements, in accordance with the comparison of Murray spinel data described above.

In fact, even the more realistic simulations resulting in Figure 3 are oversimplified, due both to the possible image shifts discussed above and to the fact that the primary beam can have non-Gaussian tails and halos as well as astigmatism. In view of all these effects, it is clear that all O isotopic anomalies obtained by raster imaging should be considered lower limits. For estimating abundances of the silicate and oxide grains obtained in our searches, we calculated detection efficiencies for each grain size by making a linear interpolation of the experimentally determined efficiencies for Murray spinel grains of average size 150 and 450 nm (Nguyen et al. 2003; Zinner et al. 2005). Measurements of presolar silicates and oxides with the Cameca IMS 1270 equipped with a silicon imaging device (SCAPS; Yurimoto et al. 2003) suffer even more from isotopic dilution effects than NanoSIMS measurements because of the more limited spatial resolution of the 1270/SCAPS analysis (Nagashima et al. 2004). As a consequence, the O isotopic ratios obtained in this way are shifted even more toward normal compositions, and the detection efficiency is lower than that obtained with NanoSIMS imaging.

Secondary ion mass spectrometry (SIMS) is a destructive measurement technique, and any subsequent grain characterization can only be performed if some material remains. In some cases, it is impossible to study a particular grain further. Fortunately, the NanoSIMS has a lower sputtering rate than other SIMS instruments, increasing the likelihood that complementary analysis techniques can be applied. The chemical compositions of presolar silicate grains have been deduced previously by obtaining energy dispersive X-ray (EDX) spectra in a scanning electron microscope (SEM; Floss & Stadermann 2004; Mostefaoui & Hoppe 2004; Mostefaoui et al. 2004; Nguyen & Zinner 2004). The excitation volume and hence lateral resolution of this technique are typically larger than the sizes of most of the presolar grains analyzed. Thus, contributing signals from surrounding grains result in uncertainties in the determined chemical compositions. Transmission electron microscope (TEM) analysis allows for the crystal

structure and chemical composition (by EDX analysis) of a grain to be established with a lateral resolution of ~1 nm, eliminating the interference from neighboring grains. The preparation of an electron-transparent grain section containing a presolar silicate grain from Acfer 094, which was carried out using focused-ion-beam (FIB) lift-out (Stroud 2003), resulted in the first TEM study of a presolar silicate grain from a meteorite. The FIB lift-out was performed using a FEI FIB 200 and an ex situ micromanipulator. The TEM studies were performed with a 200 kV JEOL 2010F TEM equipped with a Noran Vantage EDX system.

In addition, Auger spectroscopy has been applied recently to study the elemental compositions of presolar grains (Stadermann et al. 2005b). This technique makes it possible to create major element distribution images with a spatial resolution of just 10 nm. By aligning such images and secondary electron images obtained in the Auger instrument with the NanoSIMS isotopic images, it is possible to identify the presolar grains whenever they have not been completely sputtered away. One fundamental advantage of Auger spectroscopy is that no special sample preparation is required. Any sample that can be analyzed in the NanoSIMS can directly be used in the Auger spectrometer. The Auger measurements in this study were made with a PHI 700 Scanning Auger Nanoprobe at Physical Electronics in Chanhassen, Minnesota. Before the analyses, the sample surface was sputtered in the instrument for 15 s with a low-energy Ar beam to remove adhering contaminants. Secondary electron and Auger elemental distribution images were acquired at primary beam energies between 10 and 20 kV. Automated image registration was used to avoid image shifts during the acquisition of elemental maps, which took up to several hours.

## 3. RESULTS

We used the same criterion described by Zinner et al. (2003) to distinguish isotopically anomalous grains from grains having normal isotopic compositions. In this case, the range of normal isotopic ratios was determined by dividing each image into smaller areas of comparable size to the anomalous grain. Grains whose isotopic ratios are clearly distinct from the normal isotopic distribution are considered presolar. More specifically, the isotopic compositions of presolar grains had to be at least 3 $\sigma$ away from the average composition of the "normal" grains. In addition, they also had to be at least 2 $\sigma$ away from a 3 $\sigma$ ellipse around the normal grain compositions. This ellipse is centered on the average isotopic composition of the "normal" grains. A total of 19 anomalous grains in Acfer 094 and 14 anomalous grains in ALHA 77307 were identified having O isotopic ratios distinct from those of the surrounding matrix material (Figs. 4 and 5). All of these grains have sizes in the range 100–600 nm. Eleven of the grains from Acfer 094 and nine grains from ALHA 77307 have $^{24}Mg^{16}O^-/^{16}O^-$ and $^{28}Si^-/^{16}O^-$ ratios within the range for isotopically normal matrix grains, which are primarily silicates. The other anomalous grains are probably oxides. According to the $^{24}Mg^{16}O^-/^{16}O^-$ ratio, as determined by NanoSIMS analysis, five of the presolar oxides in Acfer 094 are most likely corundum or hibonite, and three are spinel. For ALHA 77307, two grains are corundum or hibonite, and three appear to be spinel. Auger analyses of six anomalous grains from ALHA 77307 indicate that one grain identified as spinel by NanoSIMS secondary ion ratios is actually a silicate grain, one Mg-poor oxide grain is a hibonite, and one grain originally identified as a silicate might actually be corundum. These results are discussed in further detail later in this section.

Abundance calculations from the study of grain size separates have large uncertainties due to errors in measuring the small mass of each separate. In addition, while the sizes of most presolar silicates are expected to fall in the range analyzed in these fractions, it is probable that some presolar silicates fall outside of this size range. The abundances of presolar silicates and oxides in Acfer 094 and ALHA 77307 were thus calculated from analyses performed on the thin sections. While this approach improves the abundance determinations, uncertainties remain due to counting statistics, difficulty in determining grain sizes, and isotopic dilution effects (see § 2). Currently, the error in grain size determination is unsystematic. For uncorrected abundances we thus report errors based on counting statistics alone, and these should be taken as lower limits. The uncertainties in abundances that are corrected for the detection efficiency include the errors from counting statistics as well as errors in determining the detection efficiency, which were derived by linear interpolation of the errors that arise

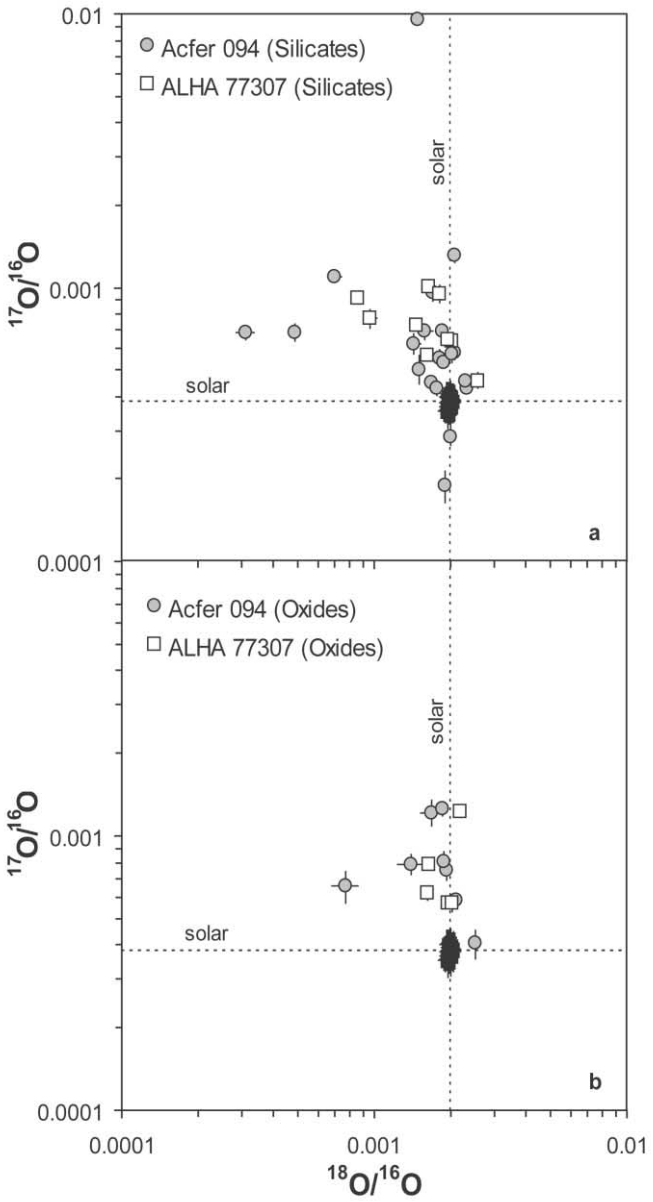


FIG. 5.—Oxygen isotopic compositions of (*a*) 29 anomalous silicate grains and (*b*) 13 anomalous oxide grains identified from the Acfer 094 and ALHA 77307 meteorites. Included are the nine presolar silicates identified by Nguyen & Zinner (2004). Also shown is the range for grains of normal isotopic compositions, which cluster around the solar composition. The compositions of the presolar candidates fall well outside the range for other matrix grains in the meteorites. Errors are given as 1 $\sigma$. The dashed lines indicate the solar ratios for $^{17}O/^{16}O$ and $^{18}O/^{16}O$.

TABLE 1
Oxygen Isotopic Ratios and Grain Sizes of Presolar Silicate Grains from Acfer 094 and ALHA 77307

| Grain | Diameter (nm) | $^{17}O/^{16}O$ ($\times10^{-4}$) | $^{18}O/^{16}O$ ($\times10^{-3}$) | $\delta^{29}Si/^{28}Si$ (‰) | $\delta^{30}Si/^{28}Si$ (‰) |
|---|---|---|---|---|---|
| A094_CG5b | 400 | 5.71 ± 0.37 | 2.03 ± 0.09 | 2 ± 18 | 29 ± 36 |
| A094_CG5a | 300 | 2.85 ± 0.21 | 2.01 ± 0.05 | 17 ± 25 | 21 ± 31 |
| A094_CG7a | 470 | 6.24 ± 0.53 | 1.44 ± 0.09 | 55 ± 25 | 19 ± 31 |
| A094_CG7b | 600 | 1.31 ± 0.77 | 2.09 ± 0.08 | 179 ± 21 | 118 ± 26 |
| A094_CG8 | 350 | 5.04 ± 0.59 | 1.51 ± 0.08 | 28 ± 29 | 29 ± 23 |
| A094_TS5 | 240 | 6.90 ± 0.44 | 1.87 ± 0.04 | −14 ± 19 | 11 ± 25 |
| A094_TS6 | 250 | 95.35 ± 1.14 | 1.50 ± 0.01 | 29 ± 43 | 43 ± 54 |
| A094_TS8 | 240 | 4.29 ± 0.25 | 1.78 ± 0.04 | 4 ± 36 | −129 ± 42 |
| A094_TS13a | 390 | 6.88 ± 0.49 | 0.49 ± 0.02 | 146 ± 23 | 77 ± 27 |
| A094_TS13b | 390 | 6.87 ± 0.40 | 0.31 ± 0.03 | ... | ... |
| A094_TS15 | 150 | 6.91 ± 0.47 | 1.59 ± 0.11 | 15 ± 39 | 25 ± 48 |
| AH77307_9 | 230 | 6.38 ± 0.31 | 2.03 ± 0.06 | ... | ... |
| AH77307_10a | 230 | 5.67 ± 0.20 | 1.62 ± 0.05 | ... | ... |
| AH77307_10b | 300 | 4.58 ± 0.31 | 2.57 ± 0.07 | ... | ... |
| AH77307_15[a] | 350 | 9.46 ± 0.68 | 1.83 ± 0.09 | ... | ... |
| AH77307_16a | 350 | 7.68 ± 0.59 | 0.97 ± 0.07 | ... | ... |
| AH77307_21a | 250 | 7.30 ± 0.41 | 1.48 ± 0.06 | ... | ... |
| AH77307_21b | 300 | 9.18 ± 0.43 | 0.86 ± 0.04 | ... | ... |
| AH77307_22 | 350 | 10.03 ± 0.41 | 1.65 ± 0.04 | ... | ... |
| AH77307_23 | 180 | 6.42 ± 0.36 | 1.95 ± 0.06 | ... | ... |
| Solar | | 3.83 | 2.01 | 0 | 0 |

Notes.—The Si isotopic ratios are also given for 10 grains in delta notation, $\delta^{i}Si/^{28}Si = \left[(^{i}Si/^{28}Si)/(^{i}Si/^{28}Si)_{\odot} - 1\right] \times 1000$. Reported errors are 1 $\sigma$. All grains from ALHA 77307 were identified in a thin section. (A094: Acfer 094, AH77307: ALHA 77307, CG: course-grained fraction, TS: thin section.)

[a] Auger analysis indicates this grain is an Fe-rich silicate, whereas NanoSIMS data inferred a spinel composition.

from the limited number of Murray spinel grains measured in single-grain analysis mode (Zinner et al. 2003, 2005).

Two separate sets of NanoSIMS analyses were performed on the ALHA 77307 thin section. The experimental conditions during acquisition of the first data set were not ideal, as the primary beam occasionally suffered substantial shifts during image acquisition, and most likely resulted in a lower detection efficiency of anomalous grains than for the second measurement session. Therefore, abundance determinations for ALHA 77307 were solely based on the second set of analyses. For each meteorite, the areas covered by the presolar silicates and oxides in the thin sections were divided by the total area analyzed. The matrix-normalized abundances of presolar silicates and oxides in Acfer 094 are 90 ± 35 and 55 ± 20 parts per million (ppm), respectively. The abundances of presolar silicates and oxides in ALHA 77307 are 95 ± 40 and 30 ± 20 ppm, respectively. After applying a correction for the detection efficiency of the imaging technique as a function of grain size, we calculate a presolar silicate abundance of 325 ± 155 ppm and a presolar oxide abundance of 360 ± 155 ppm for Acfer 094. For ALHA 77307, we obtain a corrected presolar silicate abundance of 320 ± 150 ppm and a presolar oxide abundance of 200 ± 115 ppm. The presolar silicate abundances increased by a factor of ~4, and the presolar oxide abundances increased by a factor of ~6 after the correction was applied, a consequence of the fact that the presolar oxides are on average smaller than the presolar silicate grains. When the errors in the abundance calculations are taken into account, the two meteorites have essentially the same abundances of presolar silicates and oxides.

Figure 4 shows the O isotopic ratio images and corresponding $^{24}Mg^{16}O$ and $^{28}Si$ ion images for an area containing a presolar grain from the thin section of Acfer 094. The presolar grain has a clear enrichment in $^{17}O$ and depletion in $^{18}O$. Moreover, the grain has strong signals for $^{24}Mg^{16}O$ and $^{28}Si$, indicating its silicate nature. The O isotopic ratios for all of the presolar grains found in this study, along with those identified by Nguyen & Zinner (2004), are plotted in Figure 5. They fall into the same range that has been observed for other presolar oxide grains. Also shown in this figure is the range of isotopic compositions for normal matrix grains, which is clearly distinct from the range for the presolar

TABLE 2
Oxygen Isotopic Ratios, Grain Sizes, and Preliminary Mineralogical Identifications of Presolar Oxide Grains from Acfer 094 and ALHA 77307

| Grain | Diameter (nm) | $^{17}O/^{16}O$ ($\times10^{-4}$) | $^{18}O/^{16}O$ ($\times10^{-3}$) | Mineralogy |
|---|---|---|---|---|
| A094_TS-3 | 100 | 4.05 ± 0.49 | 2.51 ± 0.08 | Spinel |
| A094_TS-3a | 160 | 7.48 ± 0.58 | 1.94 ± 0.09 | Corundum[a] |
| A094_TS-3b | 160 | 8.05 ± 0.76 | 1.90 ± 0.08 | Corundum |
| A094_TS-5 | 150 | 12.19 ± 1.35 | 1.68 ± 0.16 | Corundum |
| A094_TS-9 | 320 | 12.54 ± 0.75 | 1.87 ± 0.06 | Spinel |
| A094_TS-12 | 200 | 7.91 ± 0.67 | 1.39 ± 0.16 | Corundum |
| A094_TS-14 | 200 | 6.55 ± 0.88 | 0.77 ± 0.09 | Spinel |
| A094_TS-16 | 200 | 5.85 ± 0.20 | 2.11 ± 0.04 | Corundum |
| AH77307_6 | 300 | 6.17 ± 0.33 | 1.62 ± 0.05 | Corundum |
| AH77307_16b | 250 | 5.68 ± 0.36 | 2.03 ± 0.05 | Corundum |
| AH77307_17 | 150 | 5.71 ± 0.24 | 1.95 ± 0.03 | Hibonite[b] |
| AH77307_21c | 230 | 12.25 ± 0.59 | 2.18 ± 0.08 | Spinel |
| AH77307_29 | 200 | 7.89 ± 0.43 | 1.65 ± 0.08 | Spinel |

Notes.—The mineralogy of grains AH77307_16b and AH77307_17 were deduced by Auger microprobe analysis. The mineralogy of all other grains was inferred by the $^{24}Mg^{16}O/^{16}O$ ratio from the NanoSIMS analysis. Reported errors are 1 $\sigma$. All grains from ALHA 77307 were identified in a thin section. (A094 is Acfer 094, AH77307 is ALHA 77307, and TS is thin section.)

[a] Identification is based on the lack on MgO in the secondary ion signal. Hibonite cannot be excluded.

[b] Auger analysis indicates this grain is a hibonite grain, whereas NanoSIMS data inferred a corundum composition.

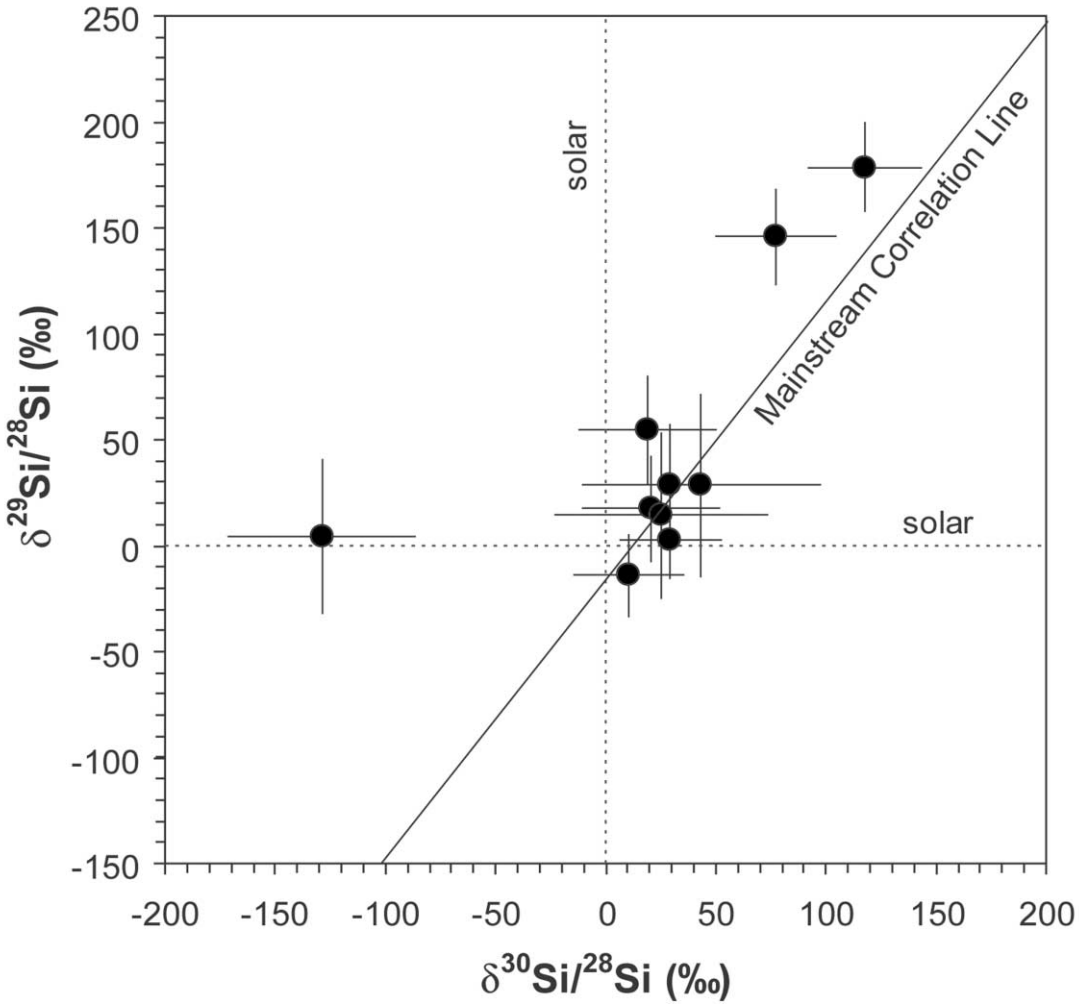


FIG. 6.—Silicon isotopic ratios given as $\delta$-values for 10 anomalous silicate grains from Acfer 094. Errors are given as 1 $\sigma$. Also shown is the silicon carbide mainstream correlation line. In general, the silicate grains fall along this correlation line, but some of the grains plot to the left of the line.

grains. The measured O isotopic ratios for the presolar silicates and oxides are given in Tables 1 and 2, respectively.

The Si isotopic compositions of 10 presolar silicates are shown in Figure 6 along with the line representing the correlation observed in the dominant "mainstream" population of presolar SiC grains (see § 4.2.2). The silicate data points primarily fall on the mainstream line, although a few plot slightly to the left. Most of the grains tend to cluster around the solar isotopic composition, which might be attributed to isotopic dilution by surrounding normal grains. As for O isotopic ratios, all Si isotopic anomalies should be taken as lower limits.

Attempts were made to produce FIB lift-out sections of six of the presolar silicate grains reported by Nguyen & Zinner (2004) from the fine-grained size separate of Acfer 094. Three sections were produced, but one grain was too small for analysis, and one section had surrounding grains attached to it. One section did provide useful information, however (Fig. 7). The TEM study of the presolar silicate grain contained in this section revealed a diffuse electron diffraction pattern, indicative of an amorphous structure. The fact that we analyzed a cross section of the grain ensures that the structural analysis is sound. The preceding NanoSIMS measurement would have amorphized only the first ~10–20 nm of the grain. In addition, the grain does not have any rims or subgrains. The EDX analysis (Fig. 8) of the presolar silicate indicates a nonstoichiometric elemental composition containing Si, O, Mg, Fe, Al, and Ca. The spectrum also shows contributions from Pt and Ga from the production of the FIB section, Cu from the TEM grid, and Cs from the implantation of primary ions during the NanoSIMS measurement. This grain was suggested to have the chemical composition of clinopyroxene based on a preliminary SEM-EDX study (Nguyen & Zinner 2004). The different conclusions drawn from the two analytical techniques illustrate the importance of FIB/TEM studies of these grains.

An example of the secondary electron images and elemental maps obtained in the scanning Auger microprobe is given in Figure 9. The presolar grain AH77307_21a, identified as a silicate in the NanoSIMS, is indicated in these images and appears as a separate grain from the surrounding matrix grains in the thin section. As can be seen in the elemental map, this grain is comparatively Mg-rich and Fe-poor, and is thus confirmed to be a Mg-rich silicate. In addition to this grain, five other grains initially identified as silicates were studied in the Auger microprobe. Two of these grains could not be distinguished from the surrounding matrix grains, and it is possible that they had been sputtered away. According to the Auger analysis, grain AH77307_21b is a Mg-rich silicate with no Fe, and grain AH77307_16a is a Mg-rich, Fe-poor silicate. These identifications are consistent with the NanoSIMS classifications. Grain AH77307_16b has a relatively high $^{28}Si^-/^{16}O^-$ ratio and a $^{24}Mg^{16}O^-/^{16}O^-$ ratio that is comparable to the image average. This grain was presumed to be a silicate, but Auger analysis

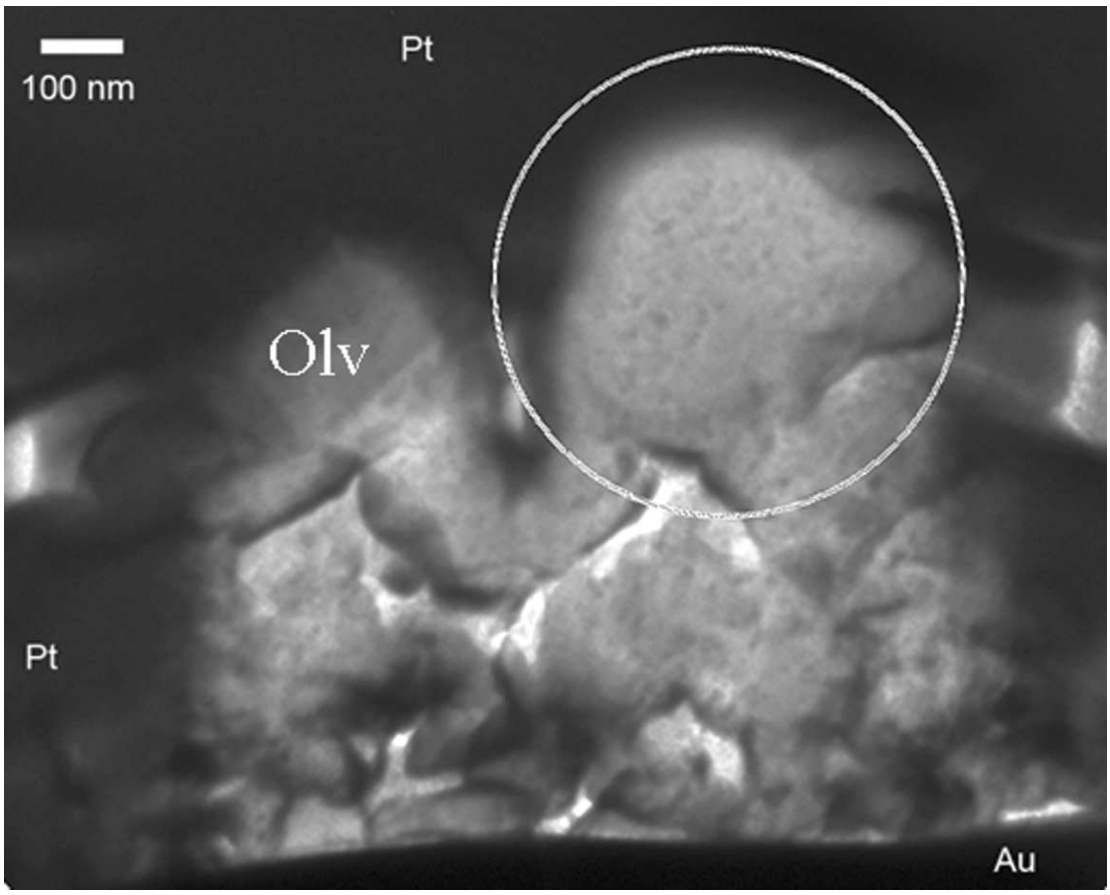


FIG. 7.—Bright-field TEM image of a FIB lift-out section produced from the Acfer 094 fine-grained size separate (grain 1 from Nguyen & Zinner 2004). The 500 nm presolar silicate is circled, and the adjoining grain was identified as an olivine. The Pt is from the production of the section, and the Au is the gold foil substrate.

indicates an Al hot spot and no Mg, suggesting corundum instead. This grain is surrounded by silicate grains and the $^{28}Si^{-}/^{16}O^{-}$ ratio obtained from NanoSIMS analysis can be attributed to signal from these neighboring silicates.

Auger analyses were also conducted on three grains that were originally classified as oxide grains according to the NanoSIMS analysis. One of these grains did not appear distinct in the Auger images and either had been sputtered away during NanoSIMS analysis or has an elemental composition that is indistinguishable from the surrounding silicate matrix. Grain AH77307_17 was initially classified as a corundum grain based on the lack of $^{28}Si^{-}$ and $^{24}Mg^{16}O^{-}$ signals in the NanoSIMS. Auger analysis of this grain showed clear signals for Ca, Al, and O, but not for Mg, Fe, or Si, and it is likely that this grain is actually hibonite ($CaAl_{12}O_{19}$). Grain AH77307_15 has a low $^{28}Si^{-}/^{16}O^{-}$ and a high $^{24}Mg^{16}O^{-}/^{16}O^{-}$ ratio relative to the average surrounding matrix material as determined by the NanoSIMS ion images. These data argue for a spinel identification. A careful alignment of the isotope ratio images with Auger elemental images, however, shows that the isotopic anomaly is carried by an Fe-rich silicate. Adjacent to this silicate grain is a Mg hot spot and an Al hot spot, which likely accounts for the initial NanoSIMS identification. Auger spectroscopy is clearly robust in elucidating the major element compositions of these small grains due to its superior lateral resolution. Since it can be used directly on the NanoSIMS sample mounts it represents a valuable companion technique to NanoSIMS analysis.

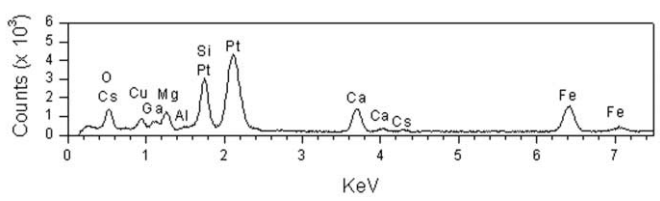


FIG. 8.—TEM-EDX analysis of a FIB lift-out section of the presolar silicate shown in Fig. 7. An electron beam of energy 200 keV was used. The spectrum indicates that the grain contains Si, O, Mg, Fe, Ca, and Al. The Cs signal comes from NanoSIMS analysis with a Cs primary ion beam. The Pt and Ga are consequences of the FIB production of the section. The Cu signal derives from the TEM grid.

## 4. DISCUSSION

Presolar silicate grains have now been identified in IDPs (Messenger et al. 2003, 2005; Floss & Stadermann 2004; Floss et al. 2006), meteorites (Mostefaoui et al. 2003, 2004; Mostefaoui & Hoppe 2004; Nagashima et al. 2004; Nguyen & Zinner 2004; Hoppe et al. 2005; Kobayashi et al. 2005; Stadermann et al. 2005a; Ebata et al. 2006; Marhas et al. 2006; Tonotani et al. 2006; Vollmer et al. 2006), and Antarctic micrometeorites (AMMs; Yada et al. 2005, 2006). We identified 19 grains in Acfer 094 and 14 grains in ALHA 77307 that have anomalous O isotopic compositions. Of these grains, 11 from Acfer 094 and nine from ALHA 77307 are Si-rich according to the $^{28}Si$ ion images. An additional 45 presolar silicates have been found in Acfer 094 (Mostefaoui & Hoppe 2004; Nagashima et al. 2004; Hoppe et al. 2005; Kobayashi et al. 2005; Stadermann et al. 2005a; Vollmer et al. 2006) and eight in ALHA 77307 (Kobayashi et al. 2005).

Although most presolar silicate grains have been identified with a NanoSIMS ion probe, they have also been identified by

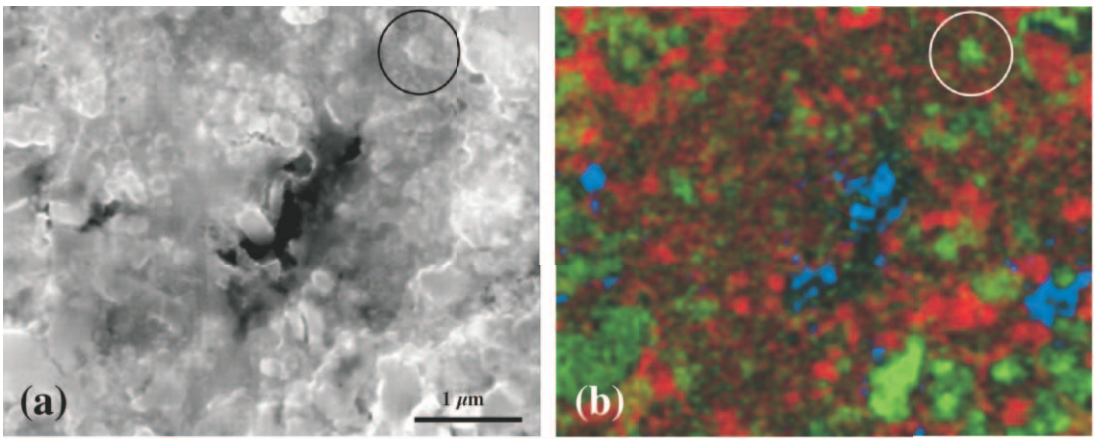


FIG. 9.—Scanning Auger microprobe images of an area on the ALHA 77307 thin section containing the presolar silicate AH77307_21a. (*a*) Secondary electron image of the area containing the presolar grain (*circled*); (*b*) composite RGB elemental Auger image; *red*: Fe, *green*: Mg, *blue*: Al. The presolar grain appears distinct from the surrounding grains in both images and clearly is enriched in Mg. The Auger analysis confirms that this grain is indeed a Mg-rich silicate.

direct ion imaging in a Cameca IMS-1270 ion microprobe equipped with a SCAPS solid-state imaging device (Nagashima et al. 2004, 2005; Kobayashi et al. 2005; Ebata et al. 2006; Tonotani et al. 2006). The spatial resolution of the IMS-1270 (~0.3–1 μm), however, is inferior to that of the NanoSIMS (~0.1 μm). Consequently, the isotopic compositions are even more diluted and many of the small anomalous grains go undetected. In the remaining discussion, we concentrate on studies that were performed with the NanoSIMS.

### 4.1. *Abundance*

All of the meteorites in which presolar silicates have been found were chosen specifically because they are good candidates for the preservation of presolar minerals that are less robust than other presolar phases already identified. In fact, many of the meteorites chosen are far from being representative samples of the chondrite class to which they belong. Thus, the difference in abundance of presolar silicates between these meteorites does not necessarily reflect any trend in the primitive state of different types of chondrites. Figure 10 gives the abundances of presolar silicates and oxides in various extraterrestrial samples. In order to obtain a meaningful comparison with the results reported by other investigators in the figure, we have not corrected the abundances for the detection efficiency, and we thus compare the raw abundances (ratio of total area of presolar grains to total area analyzed). The analyses of all materials in Figure 10*a* were performed by ion imaging in the NanoSIMS, and the detection efficiencies are likely similar. Thus, comparison of the corrected matrix-normalized silicate abundances should give the same conclusions. In Figure 10*b* the uncorrected matrix-normalized abundances of presolar oxides in Acfer 094 and ALHA 77307 are reported and compared with the abundance of presolar oxides in Murray, which were measured by single grain analysis. In this case, it may be more realistic to compare the abundance in Murray to the corrected abundances in Acfer 094 and ALHA 77307. Nevertheless, the general conclusions are not fundamentally altered in either case.

In the following discussion of presolar silicate abundances in various samples, the reported abundances have not been corrected for detection efficiency. Floss et al. (2006) report a presolar silicate abundance of ~375 ppm in isotopically primitive IDPs. This value is likely more representative than the value of ~810 ppm derived by including the data of Messenger et al. (2003), which is biased by one particularly large presolar silicate grain. As with IDPs, the abundance of presolar silicates among individual micrometeorites can vary by a wide margin. Yada et al. (2006) calculate an average abundance of ~50 ppm for AMMs. The uncorrected abundance of presolar silicates in Acfer 094 relative to the matrix material is 90 ppm and that in ALHA 77307 is 95 ppm. Presolar silicates are susceptible to destruction by parent body processing. The difference in abundances suggests that the parent bodies of IDPs are generally more primitive than those of meteorites, and perhaps of some AMMs. On the other hand, Busemann et al. (2006) concluded from a recent study of insoluble organic matter from IDPs and carbonaceous chondrites that the parent bodies of both types of extraterrestrial materials preserve primitive organics. The combined abundance of circumstellar silicates in the matrix of the ordinary chondrites Semarkona and Bishunpur has been inferred to be ~15 ppm (Mostefaoui et al. 2003, 2004). The aqueous alteration and thermal metamorphism experienced by these ordinary chondrites have almost certainly directly affected the survival of presolar silicates. Presolar silicate abundance comparisons in various meteorites can thus provide a gauge for the effects of meteorite formation histories on presolar grain survival.

The uncorrected matrix-normalized concentrations of presolar oxide grains in Acfer 094 and ALHA 77307 are 55 ± 20 and 30 ± 20 ppm, respectively. In stark contrast, the matrix-normalized abundance of presolar oxides obtained from the single grain analysis of residues from the CM2 chondrite Murray (58.8% matrix material; McSween 1979) is only ~2 ppm (Zinner et al. 2003) and that in Tieschitz (13.5% matrix material; Huss & Lewis 1995) is only ~0.4 ppm (Nittler et al. 1997). This difference is even more glaring if we compare the detection efficiency–corrected presolar oxide abundances for Acfer 094 and ALHA 77307, 360 and 200 ppm, respectively. Presolar oxide grains are more resilient than silicate grains to processing on the parent body, and we would not expect to see much variation in the abundance among different meteorites, if indeed mixing in the early solar nebula was relatively homogeneous. The large discrepancy in the oxide abundances in these meteorite samples suggests that the distribution of presolar grains in the solar nebula was not uniform among the formation regions of different meteorite classes. Interestingly, a systematic study of the abundances of presolar SiC, diamond, and graphite in meteorites of various class and petrologic type showed correlations between the abundance patterns within a meteorite class and the metamorphic history of the host meteorite (Huss & Lewis 1995). Those data suggest that all types of chondrites sampled the same mixture of presolar grains and any observed differences in presolar grain abundances between

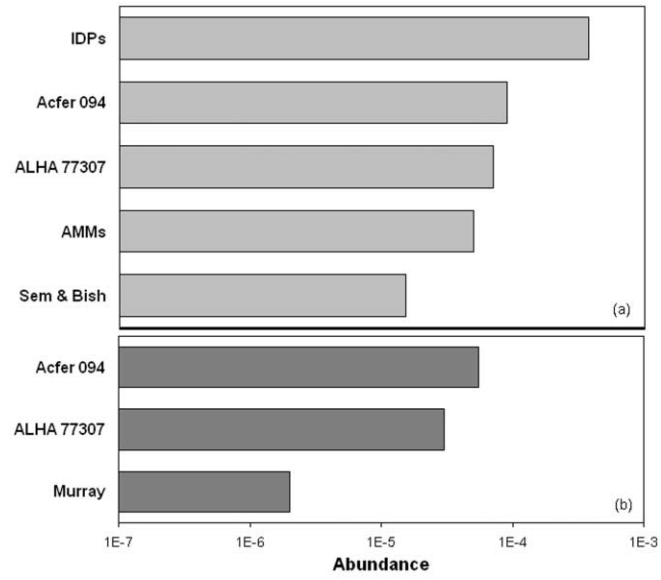


FIG. 10.—(*a*) Presolar silicate abundances in IDPs, AMMs, and meteorites from different classes. "Sem & Bish" represent the combined abundance of presolar silicates in the ordinary chondrites Semarkona and Bishunpur. All abundance estimates in meteorites are normalized to the matrix material, and no corrections for the detection efficiency have been applied. (*b*) Uncorrected matrix-normalized abundances of presolar oxides in carbonaceous chondrites. IDPs contain the greatest concentration of silicate stardust, alluding to the highly primitive nature of their parent bodies. Presolar oxide grains are much more abundant in Acfer 094 and ALHA 77307 than in Murray.

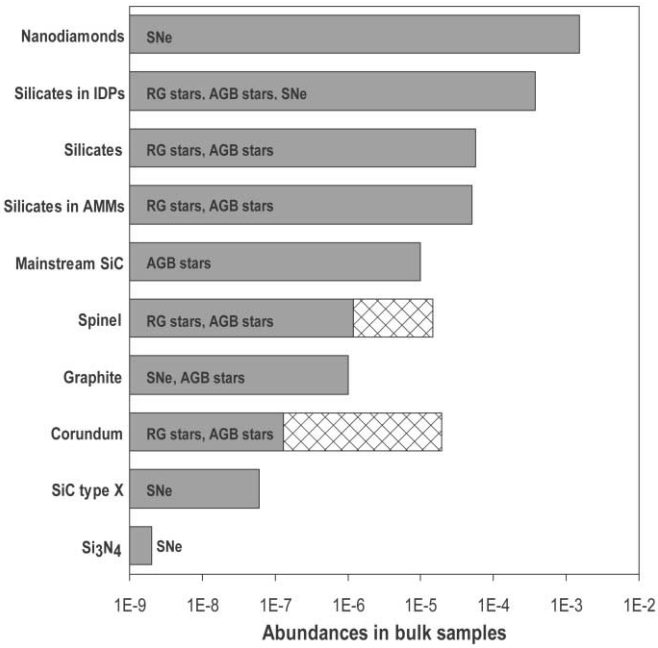


FIG. 11.—Abundances of presolar phases in bulk meteorites. Also indicated are the stellar sources for each presolar phase. Revised abundances for presolar spinel and corundum grains were made possible through the analysis of individual submicron-sized particles from the Murray carbonaceous chondrite (Zinner et al. 2003). The crosshatched bars indicate the abundance of presolar spinel and corundum in the Acfer 094 meteorite as determined by raster ion imaging in the NanoSIMS. The concentration of presolar oxides in this meteorite is larger than any previously reported oxide abundance. The abundance of presolar silicates is large relative to the concentrations of most other presolar phases, yet their discovery was made possible only recently through ion imaging in the NanoSIMS.

meteorite samples can be attributed to the degree of metamorphism (in particular, thermal processing) experienced by the meteorites. The presolar oxide abundances in the database so far seem to contradict this conclusion, unless the oxide phases are subject to alteration by thermal processing to a similar extent as silicates. However, CM2 meteorites did not experience much metamorphism and oxide grains are not expected to be highly affected by aqueous alteration. Of course, the effect of parent body metamorphism on the survival of presolar oxide grains is currently not well known. A survey of presolar oxide abundances in meteorites of various petrographic types would help to clarify the issue.

Figure 11 gives updated abundances of presolar grains in bulk samples. As in the previous figure, the presolar silicate abundances shown here have not been corrected for the detection efficiency, but the overall trends would not change. Whereas a few years ago such a chart did not even include presolar silicate grains (Zinner 1998), we now see that the presolar silicate abundance is greater than the abundances of other presolar phases, save perhaps presolar diamonds, if indeed all the meteoritic nanodiamonds are of presolar origin. This is consistent with astronomical observations, which indicate that silicate phases dominate the types of dust produced in the outflows of evolved O-rich stars and are the major solid constituent of solar system materials (Waters et al. 1996; Demyk et al. 2000). In addition, presolar oxide grains are much more abundant than they were once thought to be.

### 4.2. *Isotopic Composition*

Presolar grains present the opportunity for isotopic analysis of multiple elements in single grains. These analyses have mainly been performed in carbonaceous phases, such as SiC and graphite. More recently, many elements have also been measured in presolar oxide grains (Choi et al. 1999; Nittler et al. 2005a; Zinner et al. 2005). Similarly, the isotopic compositions of several major elements, including Si, O, and Mg, can be measured in presolar silicate grains, which originate from O-rich stars. By measuring the isotopic ratios of these elements, we can gain detailed knowledge about various nucleosynthetic processes that occur before red giants evolve into carbon stars. These ratios also reflect the effects of GCE, which established the original isotopic compositions of the parent stars.

#### 4.2.1. *Oxygen*

The O isotopic ratios are greatly affected by various astrophysical processes. These effects have previously been observed in presolar oxide grains and four groups of oxides were designated based on the O isotopic compositions of these grains (Nittler et al. 1997). Note that the grains form a continuous distribution in O isotope space, so that for some grains, assignment to a given group is somewhat ambiguous. Nonetheless, the different groups do reflect different nucleosynthetic processes and/or properties of the parent stars and are useful for purposes of discussion. The O isotopic compositions of presolar silicate grains identified in different carbonaceous and ordinary chondrites are plotted in Figure 12, along with the approximate ranges of compositions for the four oxide groups. In general, most of the presolar silicate grains fall into group 1. These grains are believed to come from red giant branch (RGB) or asymptotic giant branch (AGB) stars whose O isotopic compositions are determined by partial H burning during main-sequence evolution followed by the first (and second) dredge-up (Boothroyd & Sackmann 1999). Hydrogen burning by the CNO cycle results in zones within the star with highly enhanced $^{17}O$ and depleted $^{18}O$, relative to the starting composition. The $^{17}O/^{16}O$ ratios in the envelopes of these stars following first and second dredge-up mainly depend on stellar

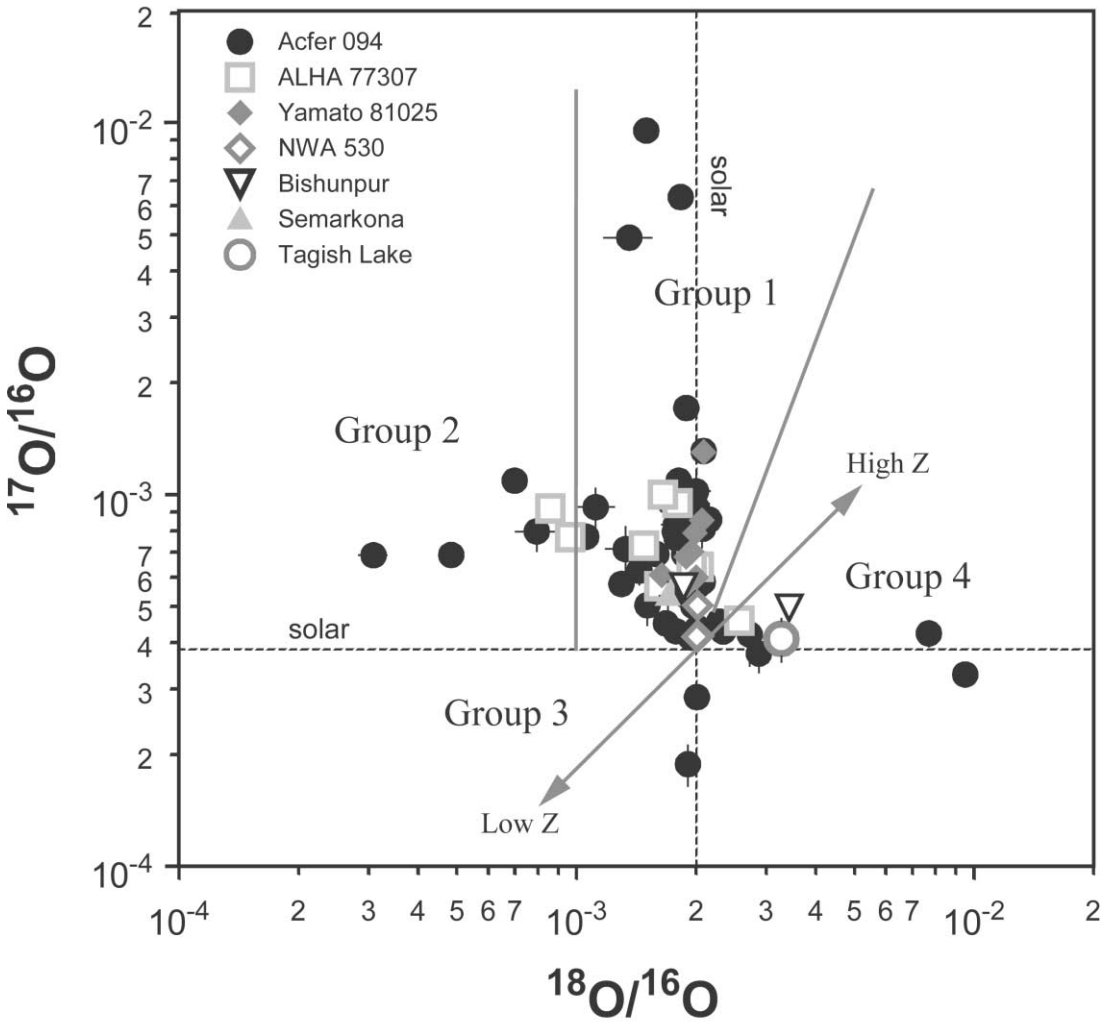


FIG. 12.—Oxygen isotopic compositions of presolar silicate grains found in different meteorites. Also shown are the approximate ranges of compositions for the four different groups of oxides defined by Nittler et al. (1997). The double-arrowed line indicates the progression from low to high metallicity (*Z*; Timmes et al. 1995). Data for Acfer 094 are from this study, Mostefaoui & Hoppe (2004), Nagashima et al. (2004), Nguyen & Zinner (2004), Hoppe et al. (2005), Stadermann et al. (2005a), and Vollmer et al. (2006). Data for NWA 530 are from Nagashima et al. (2004). Data for Semarkona are from Mostefaoui et al. (2003). Data for Bishunpur are from Mostefaoui et al. (2003, 2004). Data for Yamato 81025 and Tagish Lake are from Marhas et al. (2006). Data for ALHA 77307 are from this study. Error bars are 1 $\sigma$.

mass. For stars of up to $\sim$2.5 $M_{\odot}$, the depth of first dredge-up increases with stellar mass (Lattanzio & Boothroyd 1997), which results in higher $^{17}O/^{16}O$ envelope ratios (Boothroyd & Sackmann 1999). Above this mass, the entire $^{17}O$-rich zone of the star is mixed into an increasingly larger envelope mass and more $^{17}O$ is destroyed at the temperatures of these stars, so that the final $^{17}O/^{16}O$ ratio is lower than that in 2.5 $M_{\odot}$ stars, but still much higher than the initial ratio (Lattanzio & Boothroyd 1997; Nittler et al. 1997; Boothroyd & Sackmann 1999). Second dredge-up is significant in stars more massive than $\sim$3–4 $M_{\odot}$ (Boothroyd & Sackmann 1999; Busso et al. 1999). In contrast, $^{18}O/^{16}O$ ratios are affected much less by dredge-up episodes and, hence, do not vary much with stellar mass, but rather they most likely reflect the parent stellar metallicity (*Z*; Boothroyd et al. 1994).

The large $^{18}O$ depletions observed in group 2 grains indicate that the envelope material of their parent stars experienced partial H burning during the RGB and/or AGB phases. This could have occurred either by cool bottom processing (CBP), extra mixing that occurs when material from the envelope is cycled to regions hot enough for H burning (Wasserburg et al. 1995; Nollett et al. 2003), or by hot bottom burning (HBB) when the convective envelope extends into the H-burning shell (Boothroyd et al. 1995; Cannon et al. 1995). A CBP explanation is favored for most grains (Wasserburg et al. 1995), but HBB appears to be implicated in at least one group 2 spinel grain (Nittler et al. 2003; Lugaro et al. 2007).

The group 3 grains have $^{16}O$ excesses and have been interpreted to come from low-*Z* stars that are older and have lower mass than the parent stars of grains in the other groups. One grain with a very large $^{16}O$ excess (Fig. 13) probably originated in a supernova (SN; Nittler et al. 1998). Finally, group 4 grains are enriched in the heavy O isotopes and could come from stars with higher-than-solar metallicity, but some, especially those with the largest $^{18}O$ excesses, could have a SN origin (Choi et al. 1998).

In Figure 13 the O isotopic compositions of all presolar silicates identified to date are compared to those of presolar oxide grains identified by single grain analysis and by ion imaging in the NanoSIMS and IMS-3f ion probes. We must bear in mind when making any comparisons that the number of presolar silicates found thus far is still much smaller than the number of presolar oxides. The compositions of the presolar silicate grains span all four oxide groups and, with the exception of one highly unusual $^{18}O$-rich and $^{17}O$-poor grain (Messenger et al. 2005), do not differ drastically from the compositions of the presolar oxide

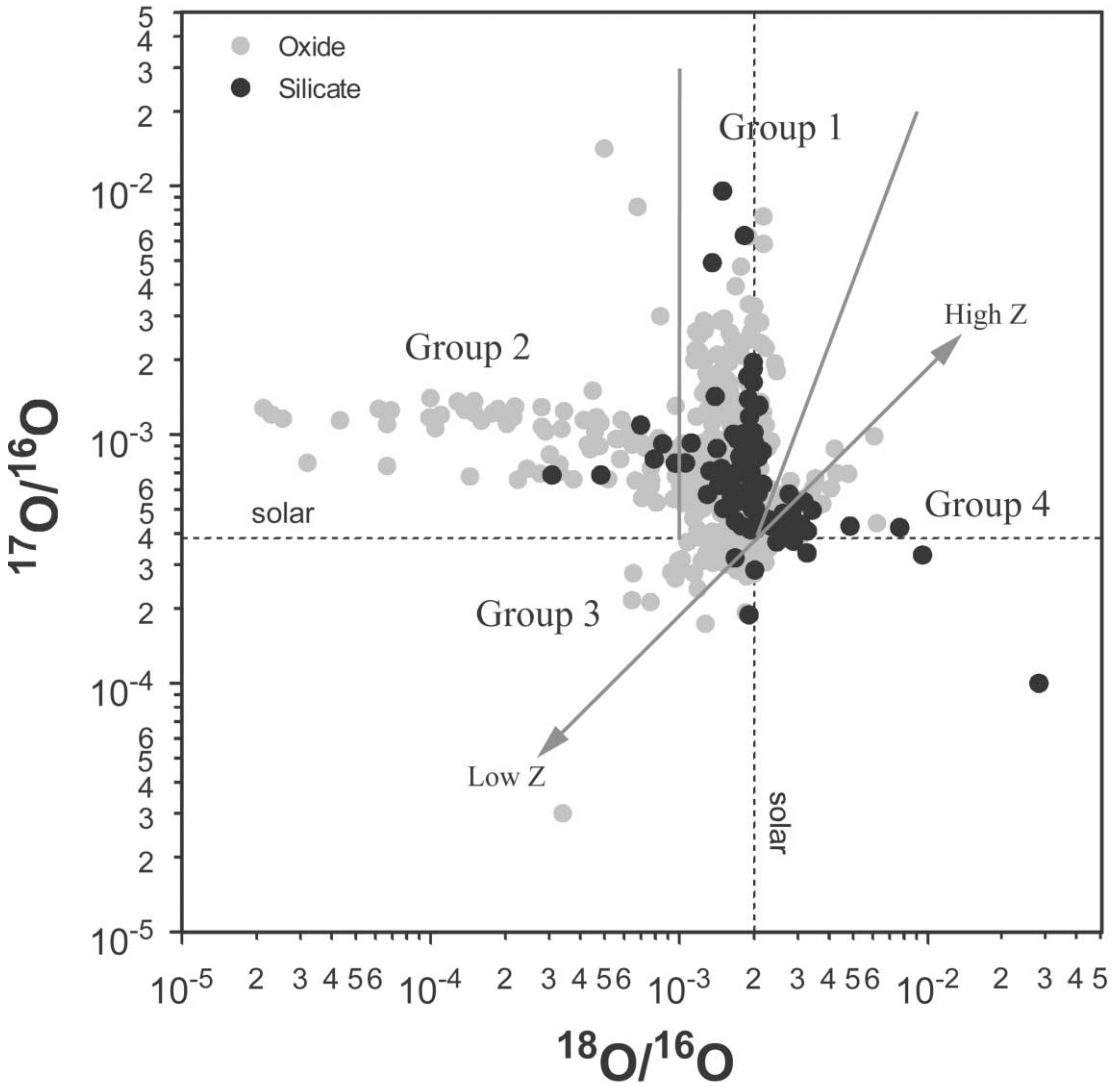


FIG. 13.—Oxygen isotopic compositions of presolar oxide grains and presolar silicate grains in meteorites, IDPs, and AMMs. The presolar oxide grains seem to have a wider range in their O isotopic ratios than presolar silicates. The O isotopic compositions of presolar silicate grains mostly fall within this range, suggesting these two presolar grain types are produced in the same types of parent sources. The reduced range of O isotopic compositions of the silicate grains is a consequence of signal dilution in the ion imaging technique (e.g., Figs. 2 and 3).

grains, indicating similar parent stellar sources. Table 3 gives the fractions of presolar oxide and silicate grains belonging to the different oxide groups arranged according to the analysis method used to identify grains. The reported errors are based solely on the number of grains identified in each category, because it is not possible to quantify the number of grains that are missed due to the isotopic dilution effects discussed previously.

For both grain types, the majority of the grains belong to group 1, with approximately equal fractions having $^{17}O/^{16}O$ ratios higher than 0.0015, indicative of formation in higher mass

TABLE 3

FRACTIONS OF PRESOLAR OXIDE AND SILICATE GRAINS IN THE DIFFERENT OXIDE GROUPS AND THE FRACTIONS THAT HAVE RELATIVELY LARGE ENRICHMENTS IN $^{17}O$ DUE TO LARGER DEPTH OF DREDGE-UP

| Analysis Technique | Grain Type | Group 1 (%) | Group 2 (%) | Group 3 (%) | Group 4 (%) | $^{17}O/^{16}O > 0.0015$ (%) |
|---|---|---|---|---|---|---|
| All techniques | Oxides | 71 ± 3 | 12 ± 1 | 7 ± 1 | 8 ± 1 | 9 ± 1 |
| | Silicates | 72 ± 8 | 5 ± 2 | 3 ± 2 | 19 ± 4 | 7 ± 3 |
| NanoSIMS | Oxides | 76 ± 4 | 8 ± 1 | 7 ± 1 | 9 ± 1 | 9 ± 1 |
| | Silicates | 70 ± 8 | 5 ± 2 | 3 ± 2 | 20 ± 4 | 7 ± 3 |
| NanoSIMS single grain | Oxides | 64 ± 5 | 16 ± 3 | 12 ± 2 | 7 ± 2 | 16 ± 3 |
| NanoSIMS imaging | Oxides | 85 ± 5 | 2 ± 1 | 3 ± 1 | 10 ± 2 | 3 ± 1 |
| | Silicates | 70 ± 8 | 5 ± 2 | 3 ± 2 | 20 ± 4 | 7 ± 3 |

NOTES.—Reported errors are based on uncertainties from counting statistics. The proportions change slightly when considering different analysis methods.

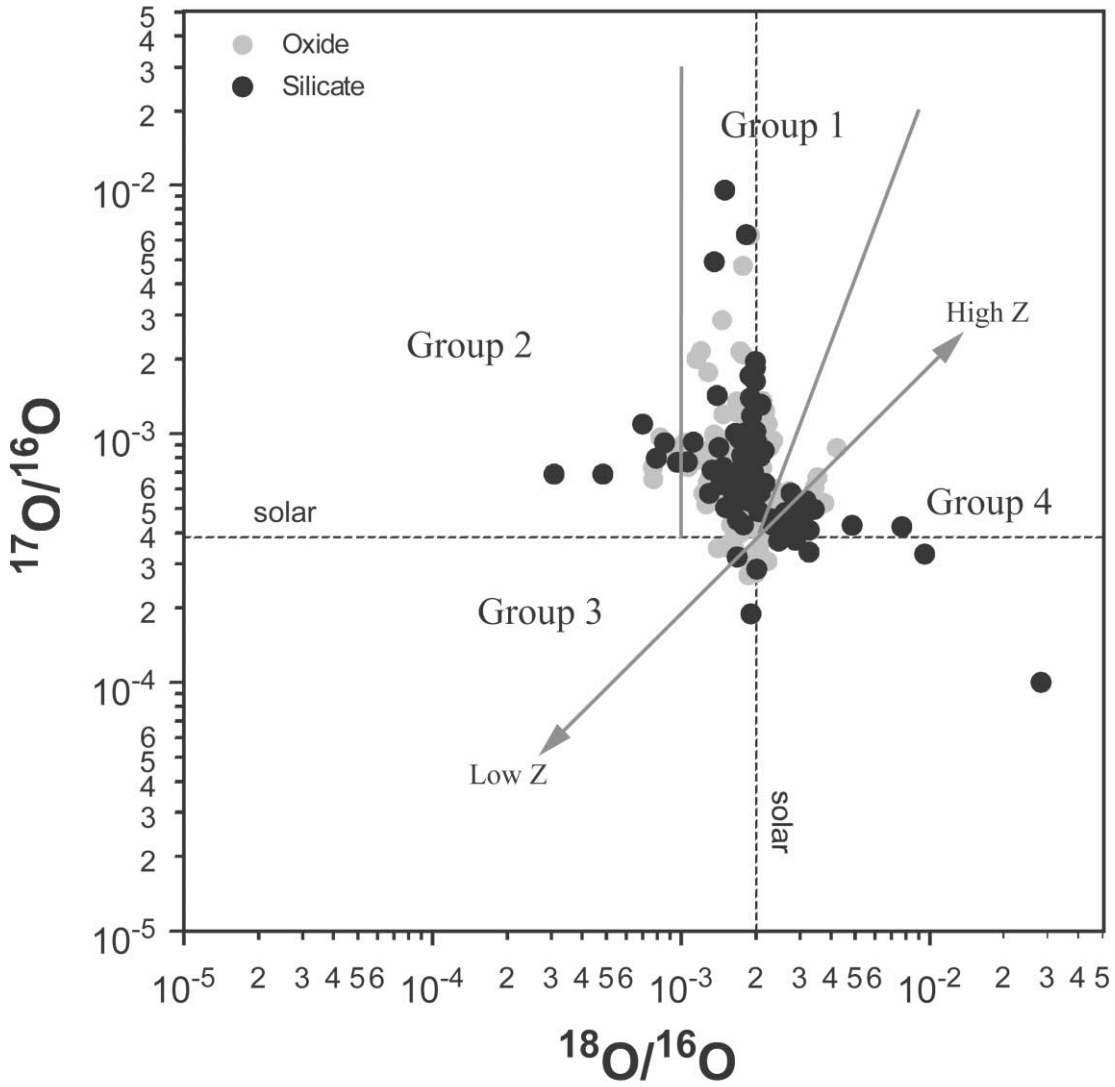


FIG. 14.—Oxygen isotopic compositions of presolar oxide and silicate grains identified by raster ion imaging in NanoSIMS. The general distributions of the ratios are very similar, but the true extent of the O isotopic compositions is not represented here. Raster ion imaging of submicron grains leads to dilution of anomalous compositions with solar isotopic composition.

stars ($1.8\ M_{\odot} < M < 4.5\ M_{\odot}$). However, in looking at the data from all analysis techniques, it appears as though a smaller fraction of silicate grains comes from low-$Z$ stars (group 3 grains), yet a larger fraction has $^{18}O$ excesses (group 4 grains). The three presolar grains having the largest $^{18}O$ enrichments are all silicates (Fig. 13; Mostefaoui & Hoppe 2004; Messenger et al. 2005; Stadermann et al. 2005a), and these grains were likely produced in SNe. One apparent difference in the O isotopic compositions of presolar silicate and oxide grains is that there is a larger fraction of presolar oxides with large depletions in $^{18}O$ (group 2 grains). Even within the different oxide groups, the presolar oxide grains are generally more depleted in $^{18}O$ than the silicate grains. This trend, however, is actually a consequence of the detection method applied. First, ion imaging in the Cameca IMS-3f ion probe creates a bias in the data set, as grains having normal $^{18}O/^{16}O$ ratios but anomalous $^{17}O/^{16}O$ ratios are overlooked (Nittler et al. 1997). Thus, the grains identified by this technique are skewed to more depleted $^{18}O$ compositions. Second, presolar grains analyzed individually also have more $^{18}O$ depleted compositions than the anomalous grains detected by raster ion imaging of tightly packed grains, but this is because of signal dilution, as previously discussed and schematically demonstrated in Figures 1–3.

Because of the biases associated with different analysis methods, a more suitable compositional comparison between presolar oxide and silicate grains is made when only those grains identified by the same method of analysis are considered. Since no presolar silicates have been discovered by single grain analysis, we compare only those grains identified by raster ion imaging in the NanoSIMS (Fig. 14). In this case, the ranges in isotopic compositions of presolar oxide and silicate grains look quite similar. The fraction of group 1 presolar oxide grains is slightly greater than that of group 1 silicate grains (Table 3). Group 3 grains make up the same percentage of both presolar oxides and presolar silicates. For group 4 the percentages of presolar silicates are greater than those of presolar oxides. Within error, the proportion of silicates in group 2 and the proportion with $^{17}O/^{16}O > 0.0015$ are the same as for presolar oxides. Of course, we must keep in mind when making such comparisons that the statistics are still very poor. Raster ion imaging in the NanoSIMS led to the identification of ~300 presolar oxide grains and 104 presolar silicate grains. As a result, the calculated fractions incur large errors. In addition, due to the isotopic dilution in ion imaging analysis, many of the "group 1" grains must actually have true compositions that fall into the group 2 range. Other "group 1" grains must have higher $^{17}O/^{16}O$ ratios

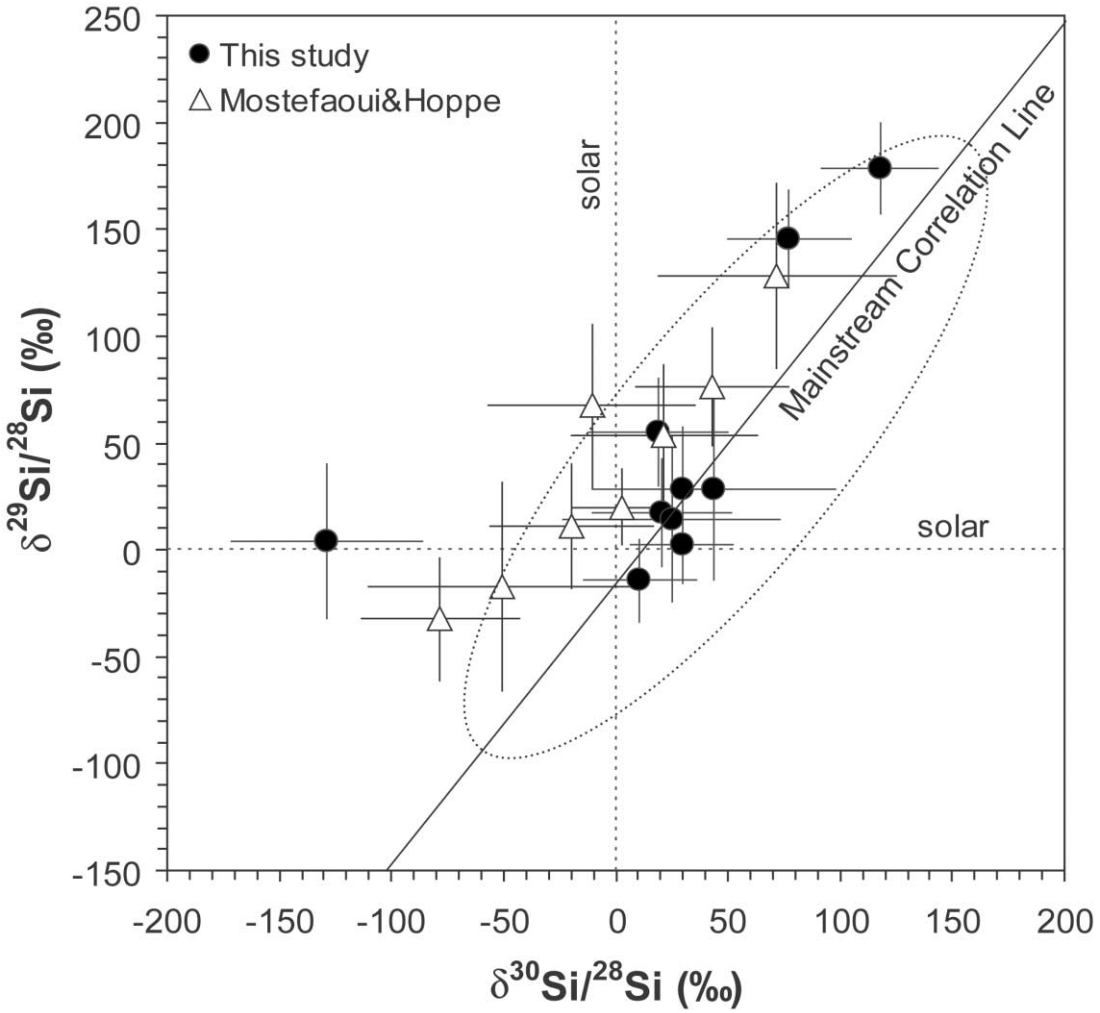


FIG. 15.—Silicon isotopic compositions of presolar silicate grains identified in meteorites (this study; Mostefaoui & Hoppe 2004). The dashed ellipse outlines the approximate range of compositions observed in mainstream SiC grains, which follow a trend indicated by the mainstream correlation line. For the most part, the data for the silicate grains fall parallel to but slightly to the left of the correlation line. These ratios most likely represent the initial Si isotopic compositions of the parent stars.

than the measured value, indicating that they formed in stars of higher mass and somewhat lower metallicity. As one can see from Figures 1 and 3, the dilution effect is smaller for grains with excesses than with depletions in one of the minor isotopes. Therefore, the shift of original group 2 grains to group 1 grains is much more significant than the shifts toward lower $^{17}O/^{16}O$ ratios.

#### 4.2.2. *Silicon*

Various types of presolar SiC grains have been identified, and they are distinguished from one another by the ranges of their C, N, and Si isotopic compositions (Hoppe & Ott 1997; Zinner 2004). The most abundant type of presolar SiC, the "mainstream" SiC, originates from low-mass AGB stars of roughly solar metallicity that have undergone enough thermal pulses followed by third dredge-up to render the stellar envelope C-rich. The Si isotopic ratios of these grains, expressed as $\delta$-values or deviations from the solar isotopic ratios in parts per thousand (‰; e.g., Table 1), fall along a correlation line of slope $\sim$1.35 on a $\delta^{29}Si/^{28}Si$ versus $\delta^{30}Si/^{28}Si$ three-isotope plot that primarily reflects the variable initial Si compositions of the parent stars (Clayton et al. 1991; Alexander 1993) as determined by GCE (Gallino et al. 1994; Timmes & Clayton 1996; Clayton & Timmes 1997a, 1997b) and local isotopic heterogeneities in the interstellar medium (ISM) attributable to SN ejecta (Lugaro et al. 1999; Nittler 2005). Also expected are small isotopic shifts from this trend along a line of slope 0.1–0.8 due to *n*-capture reactions in the He shell followed by the third dredge-up in the parent AGB stars (Gallino et al. 1990, 1994; Brown & Clayton 1992; Lugaro et al. 1999; Amari et al. 2001; Guber et al. 2003; Zinner et al. 2006). These shifts are approximately 10‰ for $^{29}Si$ and 30‰ for $^{30}Si$; the exact values vary depending on the model used.

We have measured the Si isotopic ratios in 10 presolar silicate grains (Fig. 15), and Mostefaoui & Hoppe (2004) reported Si ratios for eight presolar silicates from Acfer 094. The silicate data points span the range seen for mainstream SiC, and mostly fall parallel to, but slightly to the left of, the correlation line in the three isotope diagram. The errors are rather large, however, and the Si isotopic compositions of grains that cluster around solar could be a consequence of signal dilution. We do not expect to see isotopic shifts due to *n*-capture nucleosynthesis in presolar silicate grains, because the effects of *n*-capture on Si isotopic ratios are predicted to be noticeable at the surface only after an AGB star has become C-rich (Lugaro et al. 1999; Zinner et al. 2006). Thus, the main factor influencing the Si isotopic ratios of a given silicate grain is the initial composition of the parent star. Subsequent dredge-up of He-shell material when the star is C-rich is predicted to shift the initial Si ratios observed in silicate grains to the Si ratios seen in mainstream SiC grains.

The chemical composition of the Galaxy evolves so that the abundances of elements and isotopes heavier than H and He increase over time. This systematic trend of GCE is manifested in the initial compositions, and thus metallicities, of stars. Models of GCE predict that the initial $^{17,18}O/^{16}O$ and $^{29,30}Si/^{28}Si$ ratios of stars increase monotonically with $Z$ (Clayton 1988; Timmes et al. 1995; Alexander & Nittler 1999; Nittler & Dauphas 2006). As discussed above, the isotopic ratios, especially those of O, can be altered further by nucleosynthesis and mixing in the stars as they evolve. For RGB and AGB stars, the surface $^{17}O/^{16}O$ ratio is mainly a function of the stellar mass. In contrast, the $^{18}O/^{16}O$ ratio depends mainly on the initial composition of the star, with a small contribution from the first dredge-up, unless CBP or HBB have caused additional $^{18}O$ destruction. The O isotopic distribution of group 1 and group 3 presolar oxide grains is well explained by assuming that their parent stars did not undergo significant extra mixing (e.g., Nittler et al. 1997), and hence, the variation in the $^{18}O/^{16}O$ ratios among these grains is attributable to a range of initial stellar compositions or metallicities (Boothroyd et al. 1994). The parent stellar metallicity of a presolar grain can thus be inferred from the $^{18}O/^{16}O$ and $^{17}O/^{16}O$ ratios by interpolation of model predictions for the effects of first and second dredge-up on the O isotopic ratios of RG stars of different masses and metallicities (Boothroyd & Sackmann 1999). Note that the model of Boothroyd & Sackmann (1999) assumed a linear dependence of Galactic $^{17}O/^{16}O$ and $^{18}O/^{16}O$ on metallicity, but the precise relationship between O isotopic ratios and metallicity is unknown (see discussion in Zinner et al. [2005]). Thus, the absolute metallicity values we infer for presolar grains are subject to significant systematic uncertainty.

GCE also affects the Si isotopic system. The SiC mainstream correlation line is believed to reflect the variable initial Si compositions of the parent stars, and due to GCE, these compositions shift up the correlation line as the metallicity increases. Although some of the spread along the mainstream line might also be due to local heterogeneities in the ISM (Lugaro et al. 1999), a strong observed correlation between Si and Ti isotopic ratios in mainstream SiC grains has been used to argue that the trend is dominated by GCE (Lugaro et al. 2001; Nittler 2005). Moreover, this correlation indicates that the Ti isotopic ratios also largely reflect GCE and a correlation between $^{46}Ti/^{48}Ti$ and $^{18}O/^{16}O$ has been observed for a few presolar corundum grains (Choi et al. 1998; Alexander & Nittler 1999; Nittler 2005), although the data are sparse. Based on all of these considerations, we might therefore expect a positive correlation between the Si and O isotopic ratios of group 1 presolar silicate grains and, as a consequence, between $\delta^{29}Si/^{28}Si$ values and the parent metallicities inferred from their O isotopic ratios (Fig. 16).

Although all but one of the data points by Mostefaoui & Hoppe (2004) and those of three of our grains seem to indicate such a correlation (all having supersolar metallicity), the rest of the data points do not follow the same trend. However, there are two main difficulties with assembling and interpreting the diagram shown in Figure 16. First, the dilution of secondary ion signals by neighboring isotopically normal grains will affect both plotted variables. Dilution will of course lead to more solar-like values for all measured isotopic ratios. Because the metallicity values are inferred by subtracting a first dredge-up ($^{18}O$-depleted) component from the measured $^{18}O/^{16}O$ ratios, signal dilution increases the inferred metallicity. Thus, grains with solar Si isotopes but supersolar inferred metallicity might be explained purely by dilution effects. Moreover, if this is the case, the observed trend at supersolar metallicity could actually be a rotation of a trend with shallower slope. Second, it is possible that the parent stars of even some group 1 grains, especially those with $^{17}O/^{16}O$ ratios in the same range as those of group 2 grains, underwent CBP, leading to lower $^{18}O/^{16}O$ ratios (Nittler 2005). This would lead to inferred metallicities lower than the true ones for such grains. This is a likely explanation for the four grains in Figure 16 with inferred $Z$ lower than solar, especially since signal dilution could well have masked even larger original $^{18}O$ depletions. The fact that the grains with the largest $^{29}Si$ excesses also appear to have the highest inferred metallicities gives us confidence that GCE has indeed played a major role in establishing the isotopic compositions of the presolar grains. However, it is clear that data with better precision and accuracy, especially without significant dilution problems, are needed to make further progress.

### 4.3. *Mineralogy and Chemical Composition*

The specific mineralogy of stardust is a function of the elemental composition and the physical conditions during grain nucleation and growth in the parent stellar atmospheres. We gain knowledge about stellar nucleosynthesis and evolution through the isotopic compositions of presolar grains. By obtaining chemical and mineralogical data for the grains, a better understanding of the stellar atmosphere can be acquired. The chemical compositions of 27 presolar silicate grains have been studied in meteorites (this study; Mostefaoui & Hoppe 2004; Mostefaoui et al. 2004; Nagashima et al. 2004; Nguyen & Zinner 2004; Vollmer et al. 2006), IDPs (Messenger et al. 2003, 2005; Floss & Stadermann 2004; Floss et al. 2006), and AMMs (Yada et al. 2005, 2006). Of these, eight have compositions similar to olivine, 11 are pyroxene-like, and seven have GEMS-like compositions. GEMS (glass with embedded metal and sulfides) have been identified in IDPs and are characterized by their nonstoichiometric silicate compositions and O excesses (Bradley 1994). One Mg-rich silicate grain appears to have a corundum core (Vollmer et al. 2006). As mentioned previously, there are large uncertainties associated with chemical compositions that are determined by SEM-EDX analysis. Five presolar silicate grains have been studied by TEM, of which two are forsterite (Messenger et al. 2003, 2005), two are GEMS (Messenger et al. 2003), and one is amorphous (this study).

Of the six presolar silicate grains from Acfer 094 that were analyzed by SEM-EDX (Nguyen & Zinner 2004), four have Fe contents greater than Mg contents (atomic ratio $Mg/Fe \sim 0.5$ for three grains, $Mg/Fe \sim 0.06$ for one), but because of the small grain size, these results are uncertain. TEM-EDX analysis of one of these presolar silicate grains yields a result similar to that of the SEM-EDX analysis in that the grain exhibits a high Fe content, although it is lower than that of Mg ($Mg/Fe \sim 1.25$ for both analyses). The consistent results of these two techniques give us confidence that the other five grains that were analyzed by SEM-EDX are rich in Fe, even if we do not know the exact Mg/Fe ratio. Scanning Auger microprobe studies of presolar silicate grains from ALHA 77307 revealed two Mg-rich silicates with no Fe, one that is Mg-rich and Fe-poor, and one that is Fe-rich. The Auger spectrum for one presolar silicate grain from an IDP indicates that it is Fe-rich and Mg-poor (Floss et al. 2005). The presolar olivine grain with a SN origin also has a high Fe content as determined by TEM-EDX analysis (Messenger et al. 2005). It should be noted that the techniques used to determine the chemical compositions of these grains cannot distinguish between Fe-metal and FeO. Thus, high Fe contents indicated by the spectra could reflect high metal concentration, rather than abundant FeO.

According to astronomical spectra, the major dust species found in O-rich dust shells around evolved stars are amorphous silicates, most of which have the composition of olivine (Demyk

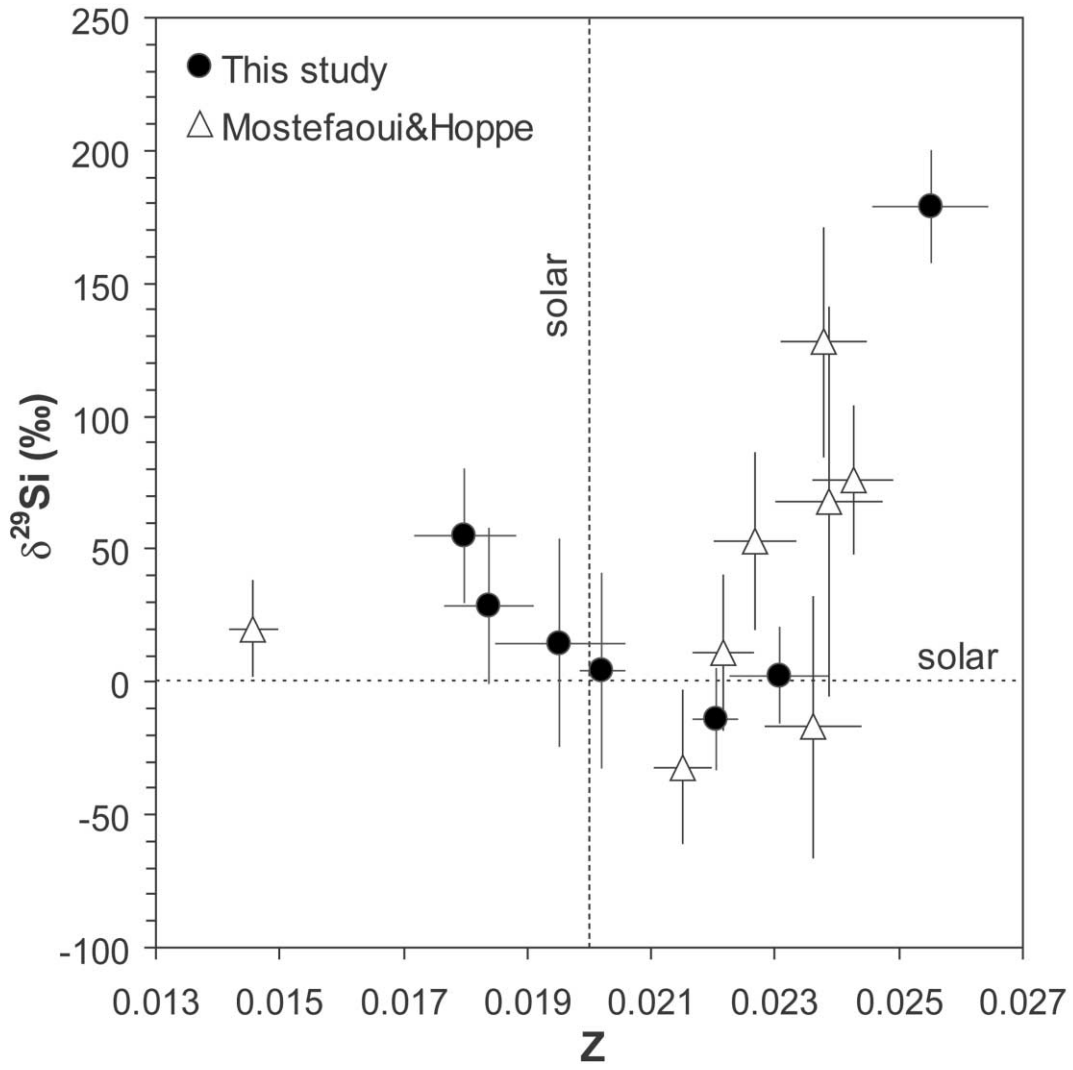


FIG. 16.—The $\delta^{29}$Si vs. inferred metallicity of the parent stars of presolar silicate grains. The metallicity is deduced from the O isotopes (primarily $^{18}O/^{16}O$ ratio) of the grains and the dredge-up models of Boothroyd & Sackmann (1999). The $\delta^{29}$Si of the Galaxy is expected to increase with increasing $Z$ because of GCE. The data for many of the grains, especially those of Mostefaoui & Hoppe (2004), more or less follow such a trend (for $Z > 0.02$), but grains with lower inferred metallicity do not follow the same trend. However, isotopic dilution from neighboring grains during raster imaging could greatly affect this plot, leading to falsely high inferred metallicity and solar Si isotopes. Moreover, extra mixing in parent stars would lead to inferred metallicity values that are too low.

et al. 2000). Moderate amounts of crystalline enstatite, forsterite, and diopside are also inferred, with most stellar sources producing 3–4 times more crystalline enstatite than crystalline olivine (Molster et al. 2002). Conversely, in the ISM the upper limit on the abundance of crystalline silicates is only ~5% (Li & Draine 2001; Kemper et al. 2005). Spectra of circumstellar environments indicate the presence of both amorphous and crystalline silicates, where the crystalline silicates contain on average <10 wt.% Fe and amorphous silicates contain more Fe (Molster et al. 1999, 2002; Demyk et al. 2000). TEM studies of presolar silicate grains also confirm the presence of crystalline and amorphous silicates having a range of Fe content.

The presolar silicate from Acfer 094 analyzed by TEM is amorphous, and thus the relatively high Fe content of this grain is not unexpected. However, it is rather surprising that four silicate grains from Acfer 094 have Mg/Fe < 1. On the other hand, only one of four silicate grains from ALHA 77307 analyzed by Auger spectroscopy is Fe-rich. The high Fe content of the silicate grains for which TEM data are not available may not be inherent to the anomalous grains, but rather could be attributed to signal from neighboring grains. Indeed, the amorphous groundmass of Acfer 094 is Fe-rich (Greshake 1997), and SEM-EDX analysis of $\sim 10 \times 10$ $\mu$m$^2$ areas of matrix material in the Acfer 094 meteorite gave Mg/Fe ~ 0.5, very similar to the ratio obtained for several of the presolar silicates. Likewise, the components of the ALHA 77307 groundmass are also Fe-rich (Brearley 1993). Another possibility suggested by Nguyen & Zinner (2004) is that Fe was introduced into the original forsterite by secondary processes taking place in the solar nebula or on the parent body. The Fe-rich rims observed around forsterite in many meteorites likely formed by condensation from a gas of higher oxygen fugacity than that of the solar nebula (Weinbruch et al. 1990). Similar circumstances could also have produced Fe-rich rims around presolar silicate grains.

Another consideration is that the high Fe content is actually a primary attribute. Whereas dust that is condensed under chemical equilibrium conditions attains an Fe content of a few percent at most, condensation under nonequilibrium conditions can

produce substantially higher Fe concentrations (Gail & Sedlmayr 1999; Ferrarotti & Gail 2001). It is actually more plausible for dust production in stellar outflows to occur out of chemical equilibrium. One of the Fe-rich presolar silicates was identified in an anhydrous IDP that presumably did not experience extensive secondary processing, and Floss et al. (2005) attribute the Fe content of this grain to nonequilibrium condensation. Moreover, Nittler et al. (2005b) reported the identification of several presolar chromite ($FeCr_2O_4$) grains with O isotopic compositions indicating an origin in AGB stars. The high Fe content of presolar silicates can thus be argued to be a primary trait, because first, spectroscopic observations indicate an abundance of amorphous silicates, which have more Fe than crystalline silicates. Second, grains with high Fe contents are predicted to condense under nonequilibrium conditions.

A further consequence of nonequilibrium condensation in stellar outflows is that olivine grains are produced in abundance, whereas pyroxene grains are relatively rare (Ferrarotti & Gail 2001). Spectroscopic observations also indicate an abundance of amorphous silicates having olivine composition (Demyk et al. 2000). However, in contrast to these expectations, in the collection of identified presolar silicate grains, eight have olivine-like compositions, and 11 have pyroxene-like compositions. It is possible that because of reduced survival of amorphous grains, we are mainly sampling the crystalline silicates, of which pyroxene is more abundant. Yet, the astronomical spectra indicate Mg-rich compositions for crystalline silicates in O-rich stellar outflows. Of course, we are still fighting with limited statistics at this point.

Various types of internal grains, most of which are TiC, have been identified in presolar graphite grains (Bernatowicz et al. 1991, 1996, 1999; Croat et al. 2003, 2005). In some cases, the TiC grains are centrally located within the graphite and presumably served as condensation nuclei. The first predicted condensation products in oxidizing environments of approximately solar composition are $Al_2O_3$ and $TiO_2$, and it has been suggested that these grains serve as seed nuclei for the condensation of silicate grains (Demyk et al. 2000). Interestingly, individual presolar $TiO_2$ grains have been identified in meteorites (Nittler & Alexander 1999; Nittler et al. 2005a). Sogawa & Kozasa (1999) calculate that both homogeneous $Al_2O_3$ and silicate grains form, in addition to heterogeneous grains having an $Al_2O_3$ core and silicate mantle. Although the heterogeneous grains are able to crystallize completely, the homogeneous grains remain amorphous. TEM analyses of two presolar $Al_2O_3$ grains that condensed in O-rich AGB stars revealed one crystalline and one amorphous grain, neither of which have evidence for subgrains (Stroud et al. 2004). The crystalline phase does bear trace amounts of Ti distributed as a solid solution. The TEM study of the presolar silicate from Acfer 094 uncovered no internal grains and that this grain is indeed amorphous. In fact, TEM analyses of other silicate grains have found no evidence of heterogeneous accretion. The data for presolar silicates support the conclusions drawn by Sogawa & Kozasa (1999).

A cautionary statement should be made here, however. In making comparisons between experimental data of pieces of stardust in the laboratory and astronomical spectra or condensation models, we must consider the uncertainties involved in each approach. Direct laboratory analyses of the products of stellar outflows provide unprecedented precision in their isotopic and elemental compositions. Still, each experimental technique applied in this study has its own limitations, which in turn place uncertainties on the data. These uncertainties are minuscule when compared to those of astronomical spectroscopy. The interpretations of the optical spectra are by no means unequivocal, but rely on comparisons with spectra of cosmic dust analogs taken in the laboratory. The exact peak positions are very sensitive to the physical conditions, as well as to the composition (the Mg/Fe ratio for instance), size, and temperature of the grains. Moreover, spectral fits are often nonunique, since different phases can have similar spectral features. The astronomical spectra and condensation models give us clues as to the types of dust expected to form around evolved stars and the conditions in which these particles formed, but we must be mindful of the uncertainties involved in their interpretation.

## 5. CONCLUSIONS

The analysis of new presolar grain types introduces a wealth of information on various astrophysical topics. This line of study is sustained by the recent discovery of presolar silicate grains and by their isotopic and mineralogical characterization. We identified 11 presolar silicates, in addition to the nine that were discovered by Nguyen & Zinner (2004), in Acfer 094, along with eight presolar oxides. In ALHA 77307, we identified nine presolar silicates and five presolar oxides. Analysis of the O isotopic compositions of these grains allows for constraint on the types of parent stellar sources, but we have yet to grasp the full extent of their isotopic distributions due not only to the limited database, but to the inherent limitations of the detection method itself. Raster ion imaging of closely packed samples leads to diluted isotopic compositions, and it is currently not possible to determine the amount of signal dilution for each particular grain. Although we succeeded in measuring the Si isotopes in 10 presolar silicates from Acfer 094, the small grain size makes the analysis of multiple isotopic systems in a single grain quite challenging.

Aside from their isotopic compositions, the mineralogy and elemental compositions of presolar grains have been investigated in order to constrain the physical conditions of the reservoirs in which they formed. The first TEM study of a presolar silicate grain from a meteorite revealed an amorphous structure and nonstoichiometric composition. Auger spectroscopy has been applied to the analysis of six presolar grains from ALHA 77307. The chemical makeup of the presolar silicates studied thus far appears to contradict the information gleaned from astronomical spectra of silicate grains in stellar environments. However, there are uncertainties involved in the interpretation of both astronomical and laboratory grain spectra. These supplementary studies are vital, however, in achieving a more comprehensive look at presolar silicate grains.

This work could not have been accomplished without the NanoSIMS ion microprobe at Washington University. The acquisition of the NanoSIMS was funded by the McDonnell Center for Space Sciences, NASA, and NSF. We thank Scott Messenger for writing the isotopic imaging data analysis program, Daniel Jayo for performing computer simulations of isotopic imaging of tightly packed grains, and Tim Smolar for keeping the NanoSIMS running. The manuscript benefited from an extensive and helpful review provided by Gary Huss. The Auger analyses were performed at Physical Electronics of Chanhassen, Minnesota. This work was supported by NASA grants NNG 05-GF81G (E. Z.) and NNG 05-GJ66G (F. J. S.).

REFERENCES


Alexander, C. M. O'D. 1993, Geochim. Cosmochim. Acta, 57, 2869
Alexander, C. M. O'D., & Nittler, L. R. 1999, ApJ, 519, 222
Amari, S., Anders, E., Virag, A., & Zinner, E. 1990, Nature, 345, 238
Amari, S., Nittler, L. R., Zinner, E., Gallino, R., Lugaro, M., & Lewis, R. S. 2001, ApJ, 546, 248
Bernatowicz, T. J., Amari, S., Zinner, E. K., & Lewis, R. S. 1991, ApJ, 373, L73
Bernatowicz, T. J., Bradley, J., Amari, S., Messenger, S., & Lewis, R. 1999, Lunar Planet. Sci. Conf., 30, 1392
Bernatowicz, T. J., Cowsik, R., Gibbons, P. C., Lodders, K., Fegley, B., Jr., Amari, S., & Lewis, R. S. 1996, ApJ, 472, 760
Bernatowicz, T. J., Fraundorf, G., Tang, M., Anders, E., Wopenka, B., Zinner, E., & Fraundorf, P. 1987, Nature, 330, 728
Boothroyd, A. I., & Sackmann, I.-J. 1999, ApJ, 510, 232
Boothroyd, A. I., Sackmann, I.-J., & Wasserburg, G. J. 1994, ApJ, 430, L77
———. 1995, ApJ, 442, L21
Bradley, J. P. 1994, Science, 265, 925
Brearley, A. J. 1993, Geochim. Cosmochim. Acta, 57, 1521
Brown, L. E., & Clayton, D. D. 1992, ApJ, 392, L79
Busemann, H., Young, A. F., Alexander, C. M. O'D., Hoppe, P., Mukhopadhyay, S., & Nittler, L. R. 2006, Science, 312, 727
Busso, M., Gallino, R., & Wasserburg, G. J. 1999, ARA&A, 37, 239
Cannon, R. C., Frost, C. A., Lattanzio, J. C., & Wood, P. R. 1995, in AIP Conf. Proc. 327, Nuclei in the Cosmos III, ed. M. Busso, R. Gallino, & C. M. Raiteri (New York: AIP), 469
Choi, B.-G., Huss, G. R., Wasserburg, G. J., & Gallino, R. 1998, Science, 282, 1284
Choi, B.-G., Wasserburg, G. J., & Huss, G. R. 1999, ApJ, 522, L133
Clayton, D. D. 1988, ApJ, 334, 191
Clayton, D. D., Obradovic, M., Guha, S., & Brown, L. E. 1991, Lunar Planet. Sci. Conf., 22, 221
Clayton, D. D., & Timmes, F. X. 1997a, in AIP Conf. Proc. 402, Astrophysical Implications of the Laboratory Study of Presolar Materials, ed. T. J. Bernatowicz & E. Zinner (New York: AIP), 237
———. 1997b, ApJ, 483, 220
Croat, T. K., Bernatowicz, T., Amari, S., Messenger, S., & Stadermann, F. J. 2003, Geochim. Cosmochim. Acta, 67, 4705
Croat, T. K., Stadermann, F. J., & Bernatowicz, T. J. 2005, ApJ, 631, 976
Demyk, K., Dartois, E., Wiesemeyer, H., Jones, A. P., & d'Hendecourt, L. 2000, A&A, 364, 170
Ebata, S., Nagashima, K., Itoh, S., Kobayashi, S., Sakamoto, N., Fagan, T. J., & Yurimoto, H. 2006, Lunar Planet. Sci. Conf., 37, 1619
Ferrarotti, A. S., & Gail, H.-P. 2001, A&A, 371, 133
Floss, C., & Stadermann, F. J. 2004, Lunar Planet. Sci. Conf., 35, 1281
Floss, C., Stadermann, F. J., Bradley, J. P., Dai, Z. R., Bajt, S., Graham, G., & Lea, A. S. 2006, Geochim. Cosmochim. Acta, 70, 2371
Floss, C., Stadermann, F. J., Nguyen, A., Zinner, E., & Lea, A. S. 2005, Meteoritics Planet. Sci., 40, Abs. 5093
Gail, H.-P., & Sedlmayr, E. 1999, A&A, 347, 594
Gallino, R., Busso, M., Picchio, G., & Raiteri, C. M. 1990, Nature, 348, 298
Gallino, R., Raiteri, C. M., Busso, M., & Matteucci, F. 1994, ApJ, 430, 858
Greshake, A. 1997, Geochim. Cosmochim. Acta, 61, 437
Guber, K. H., Koehler, P. E., Derrien, H., Valentine, T. E., Leal, L. C., Sayer, R. O., & Rauscher, T. 2003, Phys. Rev. C, 67, 062802
Hoppe, P., Mostefaoui, S., & Stephan, T. 2005, Lunar Planet. Sci. Conf., 36, 1301
Hoppe, P., & Ott, U. 1997, in AIP Conf. Proc. 402, Astrophysical Implications of the Laboratory Study of Presolar Materials, ed. T. J. Bernatowicz & E. Zinner (New York: AIP), 27
Huss, G. R., Fahey, A. J., Gallino, R., & Wasserburg, G. J. 1994, ApJ, 430, L81
Huss, G. R., & Lewis, R. S. 1995, Geochim. Cosmochim. Acta, 59, 115
Hutcheon, I. D., Huss, G. R., Fahey, A. J., & Wasserburg, G. J. 1994, ApJ, 425, L97
Kemper, F., Vriend, W. J., & Tielens, A. G. G. M. 2005, ApJ, 633, 534
Kobayashi, S., Tonotani, A., Sakamoto, N., Nagashima, K., Krot, A. N., & Yurimoto, H. 2005, Lunar Planet. Sci. Conf., 36, 1931
Krestina, N., Hsu, W., & Wasserburg, G. J. 2002, Lunar Planet. Sci. Conf., 33, 1425
Lattanzio, J. C., & Boothroyd, A. I. 1997, in AIP Conf. Proc. 402, Astrophysical Implications of the Laboratory Study of Presolar Materials, ed. T. J. Bernatowicz & E. Zinner (New York: AIP), 85
Lewis, R. S., Tang, M., Wacker, J. F., Anders, E., & Steel, E. 1987, Nature, 326, 160
Li, A., & Draine, B. T. 2001, ApJ, 550, L213
Lugaro, M., Gallino, R., Zinner, E., & Amari, S. 2001, Meteoritics Planet. Sci. Suppl., 36, 118
Lugaro, M., Karakas, A. I., Nittler, L. R., Alexander, C. M. O'D., Hoppe, P., Iliadis, C., & Lattanzio, J. C. 2007, A&A, 461, 657
Lugaro, M., Zinner, E., Gallino, R., & Amari, S. 1999, ApJ, 527, 369
Malfait, K., Waelkens, C., Waters, L. B. F. M., Vandenbussche, B., Huygen, R., & de Graauw, T. 1998, A&A, 332, L25
Marhas, K. K., Hoppe, P., Stadermann, F. J., Floss, C., & Lea, A. S. 2006, Lunar Planet. Sci. Conf., 37, 1959
McSween, H. Y., Jr. 1979, Geochim. Cosmochim. Acta, 43, 1761
Messenger, S., Keller, L. P., & Lauretta, D. S. 2005, Science, 309, 737
Messenger, S., Keller, L. P., Stadermann, F. J., Walker, R. M., & Zinner, E. 2003, Science, 300, 105
Molster, F. J., Waters, L. B. F. M., Tielens, A. G. G. M., Koike, C., & Chihara, H. 2002, A&A, 382, 241
Molster, F. J., et al. 1999, Nature, 401, 563
Mostefaoui, S., & Hoppe, P. 2004, ApJ, 613, L149
Mostefaoui, S., Hoppe, P., Marhas, K. K., & Gröner, E. 2003, Meteoritics Planet. Sci., 38, Abs. 5185
Mostefaoui, S., Marhas, K. K., & Hoppe, P. 2004, Lunar Planet. Sci. Conf., 35, 1593
Nagashima, K., Krot, A. N., & Yurimoto, H. 2004, Nature, 428, 921
Nagashima, K., Sakamoto, N., & Yurimoto, H. 2005, Lunar Planet. Sci. Conf., 36, 1671
Nguyen, A. N., & Zinner, E. 2004, Science, 303, 1496
Nguyen, A. N., Zinner, E., & Lewis, R. S. 2003, Publ. Astron. Soc. Australia, 20, 382
Nittler, L. R. 2003, Earth Planet. Sci. Lett., 209, 259
———. 2005, ApJ, 618, 281
Nittler, L. R., & Alexander, C. M. O'D. 1999, Lunar Planet. Sci. Conf., 30, 2041
Nittler, L. R., Alexander, C. M. O'D., Gao, X., Walker, R. M., & Zinner, E. K. 1994, Nature, 370, 443
———. 1997, ApJ, 483, 475
Nittler, L. R., Alexander, C. M. O'D., Stadermann, F. J., & Zinner, E. K. 2005a, Lunar Planet. Sci. Conf., 36, 2200
———. 2005b, Meteoritics Planet. Sci., 40, Abs. 5208
Nittler, L. R., Alexander, C. M. O'D., Wang, J., & Gao, X. 1998, Nature, 393, 222
Nittler, L. R., & Dauphas, N. 2006, in Meteorites and the Early Solar System II, ed. D. S. Lauretta & H. Y. McSween, Jr. (Tucson: Univ. Arizona Press), 127
Nittler, L. R., Hoppe, P., Alexander, C. M. O'D., Busso, M., Gallino, R., Marhas, K. K., & Nollett, K. 2003, Lunar Planet. Sci. Conf., 34, 1703
Nollett, K. M., Busso, M., & Wasserburg, G. J. 2003, ApJ, 582, 1036
Sogawa, H., & Kozasa, T. 1999, ApJ, 516, L33
Stadermann, F. J., Floss, C., Bland, P. A., Vicenzi, E. P., & Rost, D. 2005a, Lunar Planet. Sci. Conf., 36, 2004
Stadermann, F. J., Floss, C., Zinner, E., Nguyen, A., & Lea, A. S. 2005b, Meteoritics Planet. Sci., 40, Abs. 5123
Strebel, R., Hoppe, P., & Eberhardt, P. 1996, Meteoritics Planet. Sci. Suppl., 31, 136
Stroud, R. M. 2003, in Workshop on Cometary Dust in Astrophysics, ed. D. E. Brownlee, L. P. Keller, & S. R. Messenger (Houston: LPI), A6011
Stroud, R. M., Nittler, L. R., & Alexander, C. M. O'D. 2004, Science, 305, 1455
Tang, M., & Anders, E. 1988, Geochim. Cosmochim. Acta, 52, 1235
Timmes, F. X., & Clayton, D. D. 1996, ApJ, 472, 723
Timmes, F. X., Woosley, S. E., & Weaver, T. A. 1995, ApJS, 98, 617
Tonotani, A., Kobayashi, S., Nagashima, K., Sakamoto, N., Russell, S. S., Itoh, S., & Yurimoto, H. 2006, Lunar Planet. Sci. Conf., 37, 1539
Vollmer, C., Hoppe, P., Brenker, F. E., & Palme, H. 2006, Lunar Planet. Sci. Conf., 37, 1284
Waelkens, C., et al. 1996, A&A, 315, L245
Wasserburg, G. J., Boothroyd, A. I., & Sackmann, I.-J. 1995, ApJ, 447, L37
Waters, L. B. F. M., et al. 1996, A&A, 315, L361
Weinbruch, S., Palme, H., Müller, W. F., & El Goresy, A. 1990, Meteoritics, 25, 115
Yada, T., Stadermann, F. J., Floss, C., Zinner, E., Nakamura, T., Noguchi, T., & Lea, A. S. 2006, Lunar Planet. Sci. Conf., 37, 1470
Yada, T., et al. 2005, Lunar Planet. Sci. Conf., 36, 1227
Yurimoto, H., Nagashima, K., & Kunihiro, T. 2003, Appl. Surface Sci., 203–204, 793
Zinner, E. 1998, Annu. Rev. Earth Planet. Sci., 26, 147
———. 2004, in Treatise on Geochemistry Vol. 1, Meteorites, Planets, and Comets, ed. A. M. Davis (Oxford: Elsevier), 17
Zinner, E., Amari, S., Guinness, R., Nguyen, A., Stadermann, F., Walker, R. M., & Lewis, R. S. 2003, Geochim. Cosmochim. Acta, 67, 5083
Zinner, E., Nittler, L. R., Gallino, R., Karakas, A. I., Lugaro, M., Straniero, O., & Lattanzio, J. C. 2006, ApJ, 650, 350
Zinner, E., Nittler, L. R., Hoppe, P., Gallino, R., Straniero, O., & Alexander, C. M. O'D. 2005, Geochim. Cosmochim. Acta, 69, 4149